

## SEARCH AND STUDY OF ULTRACOMPACT H II REGIONS

D. Quiroga-González<sup>1,2</sup>, M. A. Trinidad<sup>1,3</sup>, E. de la Fuente<sup>4</sup>, J. M. Masqué<sup>1</sup>, and T. Rodríguez-Esnard<sup>5</sup>

*Received March 1 2023; accepted June 12 2023*

### ABSTRACT

We present results from a sample of 106 high-luminosity IRAS sources observed with the Very Large Array in the B and C configurations. 96 sources were observed in the X-band and 52 in the K-band, with 42 of them observed at both wavelengths. We also used previously published observations in the C-band for 14 of them. The detection rate of sources with 3.6 cm continuum emission was  $\approx 25\%$ , while only 10% have emission at 1.3 cm. In order to investigate the nature of these sources, their physical parameters were calculated mainly using the 3.6 cm continuum emission, and for sources detected at two wavelengths, we used the best fit of three H II region models with different geometries. As a final result, we present a catalog of the detected sources, which includes their basic physical parameters for further analysis. The catalog contains 17 ultracompact H II regions and 3 compact H II regions.

### RESUMEN

Presentamos resultados de una muestra de 106 fuentes IRAS de alta luminosidad observadas con el interferómetro Very Large Array en las configuraciones B y C. 96 fuentes se observaron en la banda X y 52 en la banda K, con 42 de ellas observadas en ambas longitudes de onda. También usamos observaciones previamente publicadas en la banda C para 14 de ellas. La tasa de detección de fuentes con emisión de continuo a 3.6 cm fue del  $\approx 25\%$ , mientras que sólo un 10% tienen emisión a 1.3 cm. Para investigar la naturaleza de estas fuentes se calcularon sus parámetros físicos usando principalmente la emisión de continuo a 3.6 cm y para fuentes detectadas en dos longitudes de onda usamos el mejor ajuste de tres modelos de regiones H II con diferentes geometrías. Como resultado final, presentamos un catálogo de las fuentes detectadas y proporcionamos sus parámetros físicos básicos para su posterior análisis. El catálogo contiene 17 regiones H II ultracompactas y 3 regiones H II compactas.

*Key Words:* HII regions — ISM: general — radio continuum: ISM — stars: early type — stars: formation

### 1. INTRODUCTION

The study of high-mass star formation is crucial for understanding the physical and chemical evolution of galaxies. Because forming massive stars takes  $\approx 10^6$  yr, the process of high mass star formation is less understood than the formation of low-mass stars (time-scales of  $\approx 10^9$  yr). Currently, it is

not completely clear how massive stars form, being monolithic collapse, protostar collision and/or coalescence, and competitive accretion the most widely accepted models (see Motte, Bontemps & Louvet 2018, and references therein). Studying the evolution of the earliest phases of high-mass star formation is key to understanding how this process occurs. In this sense, two of the earliest phases of massive star formation are the young stellar object and the H II region (e.g. Garay & Lizano 1999). While both stages have been extensively studied, new questions continue to arise about their formation and evolution process. Further study of these evolutionary phases will undoubtedly contribute to a better understand-

<sup>1</sup>Departamento de Astronomía, Universidad de Guanajuato, Guanajuato, México.

<sup>2</sup>Universidad Autónoma Metropolitana, México.

<sup>3</sup>Corresponding author.

<sup>4</sup>Departamento de Física, CUCEI, Universidad de Guadalajara, Jalisco, México.

<sup>5</sup>Instituto de Geofísica y Astronomía de la República de Cuba.

TABLE 1  
PHYSICAL PARAMETERS OF H II REGIONS<sup>a</sup>

Type of H II region	Size (pc)	EM (cm <sup>-6</sup> pc)	$n_e$ (cm <sup>-3</sup> )	$M_{\text{H II}}$ (M <sub>⊙</sub> )	Reference <sup>b</sup>
Hypercompact	≈ 0.003	≥ 10 <sup>10</sup>	≥ 10 <sup>6</sup>	≈ 10 <sup>-3</sup>	1
Ultracompact	≲ 0.1	≥ 10 <sup>7</sup>	≥ 10 <sup>4</sup>	≈ 10 <sup>-3</sup>	2,3
Compact	≲ 0.5	≥ 10 <sup>7</sup>	≥ 5×10 <sup>3</sup>	≈ 1	4
Ultracompact with Extended Emission	1–20	10 <sup>4</sup> –10 <sup>5</sup>	≥ 10 <sup>2</sup> –10 <sup>3</sup>	5–10 <sup>3</sup>	5

<sup>a</sup>Adapted from Kurtz & Franco (2002); de la Fuente et al. (2020b).

<sup>b</sup>1.- Sewilo et al. (2008, 2004), 2.- Wood & Churchwell (1989), 3.- Kurtz et al. (1994), 4.- Lumsden et al. (2013), 5.- (de la Fuente et al. 2020a,b, and references therein).

ing of massive star formation and provide evidence for or against the proposed models.

One way to contribute to solving the puzzle of high-mass star formation is to study the H II regions related to this process: the hypercompact (HC), ultra-compact (UC), and compact H II regions. These objects are thought to be related to the evolutionary sequence as the massive star approaches the zero-age main sequence or ZAMS (e.g. Beuther et al. 2007, and references therein). The physical parameters that define HC H II, UC H II, and compact H II regions following this evolutionary sequence are shown in Table 1.

On the other hand, density gradients are highly noticeable in H II regions (e.g. de Pree, Rodriguez, & Goss 1995; Jaffe & Martin-Pintado 1999; Franco et al. 2000a,b, 2001; Phillips 2007, 2008). These gradients are important and useful to describe the dynamics of an H II region. For example, density gradients with a power law of  $n_e \propto r^\beta$ , where  $r$  is the distance from the ionization front, accurately describe expanding H II regions when  $\beta \gtrsim 1.5$  (e.g. Franco, Tenorio-Tagle, and Bodenheimer 1990; Franco et al. 2000a,b, 2001, and references therein). Thus, the presence of these gradients should be taken into consideration in models and studies of HC H II, UC H II, and compact H II regions.

In order to advance in the understanding of the earliest stages of the high-mass star formation process and to find evidence in favor of one of the models mentioned above, we perform a physical characterization of the ionized gas in a sample of 106 IRAS sources to identify H II regions in their different evolutionary stages. We calculate physical parameters at 3.6 cm in the standard way, and we apply density gradient models for sources with multiple wavelength observations. We aim to confirm if they are H II regions and, if applicable, to determine their

nature and classify them as HC H II, UC H II, or compact H II region, taking into consideration the presence of protostellar thermal jets.

The sample, radio continuum observations, and data reduction are described in § 2. Results and discussion are presented in § 3 and § 4, respectively. Finally, we give the conclusions in § 5 and individual sources comments are provided in Appendix A.

## 2. OBSERVATIONS

We retrieve 3.6 and 1.3 cm data for a sample of 104 IRAS sources from the Very Large Array (VLA<sup>6</sup>) archive using the B and C configurations, respectively (unpublished data from the AC295 project; P.I. Ed Churchwell). Out of the 104 sources, 94 were observed in the X band and 52 in the K band, with 42 observed at both wavelengths. We also included two sources (IRAS 18094-1823 and G45.47+0.05) observed in the X band with the VLA D configuration (AK559 project; P.I. Stan Kurtz; see de la Fuente et al. 2018, 2020a), bringing the final sample to 106 sources. The observations of the AC295 project, at both wavelengths, were carried out in snapshot mode using a bandwidth of 50 MHz, with an integration time of 5 and 10 minutes for 3.6 and 1.3 cm, respectively, over a time span of about 4.5 months (1992 January and May) for both bands. Table 2 lists the 106 sources in the sample observed at 3.6 and 1.3 cm. Additionally, we also used 6 cm data, observed with the VLA-B and reported by Urquhart et al. (2009), for some sources detected at 3.6 and/or 1.3 cm. All sources in the sample are located in star-forming regions associated with high luminosity IRAS sources ( $L_{\text{FIR}} \gtrsim 500 L_\odot$ ), and are situated more than 1 kpc away. They cover a range from ≈ 21<sup>h</sup> to 08.5<sup>h</sup> in right ascension (J2000), and from ≈ -41° to 66° in

<sup>6</sup>The National Radio Astronomy Observatory is a facility of the National Science Foundation operated under cooperative agreement by Associated Universities, Inc.

TABLE 2

THE SAMPLE OF 106 IRAS SOURCES: 96 OBSERVED AT 3.6 CM, 10 AT 1.3 CM, AND 42 OBSERVED AT BOTH WAVELENGTHS

IRAS Source	RA (J2000) (h:m:s)	DEC (J2000) (°: ′: ″)	IRAS Source	RA (J2000) (h:m:s)	DEC (J2000) (°: ′: ″)	IRAS Source	RA (J2000) (h:m:s)	DEC (J2000) (°: ′: ″)
00117+6412*	00:14:27.72	64:28:46.3	05554+2013	05:58:24.56	20:13:57.5	07528-3441	07:54:49.97	-34:49:45.9
00338+6312**	00:36:47.51	63:29:02.1	06055+2039*	06:08:32.82	20:39:16.2	07530-3436**	07:54:56.18	-34:49:38.3
00412+6638*	00:44:15.23	66:54:40.6	06073+1249*	06:10:12.43	12:48:45.5	08007-2829	08:02:46.36	-28:25:47.4
00468+6508	00:49:55.82	65:43:38.7	06084+1727	06:11:24.52	17:26:26.5	08008-3423	08:02:42.30	-34:31:46.8
00468+6527**	00:49:55.82	65:43:38.7	06089+1727**	06:11:44.41	17:26:05.1	08088-3554*	08:10:43.49	-36:03:29.8
00556+6048	00:58:40.13	61:04:44.0	06103+1523	06:13:18.21	15:23:16.1	08140-3556	08:15:58.98	-36:08:20.0
00578+6233	01:00:55.81	62:49:28.5	06104+1524A**	06:13:21.32	15:23:56.9	08159-3543	08:17:52.89	-35:52:49.9
01045+6505*	01:07:50.70	65:21:21.4	06105+1756*	06:13:28.33	17:55:29.5	08189-3602*	08:20:47.86	-36:12:34.4
01133+6434*	01:16:37.39	64:50:38.8	06114+1745*	06:14:23.69	17:44:36.5	08212-4146	08:23:02.96	-41:55:48.5
02044+6031*	02:08:05.05	60:45:56.7	06155+2319A	06:18:35.15	23:18:11.4	08245-4038*	08:26:17.70	-40:48:35.1
02395+6244	02:43:28.72	62:57:05.3	06208+0957*	06:23:34.41	09:56:22.1	08274-4111	08:29:13.94	-41:10:44.4
02437+6145*	02:47:40.43	61:58:26.3	06306+0437*	06:33:16.36	04:34:56.8	18094-1823 <sup>a</sup>	18:12:23.63	-18:22:53.7
02455+6034	02:49:23.23	60:47:01.2	06331+1102	06:35:56.01	11:00:17.5	19120+1103 <sup>b</sup>	19:14:25.67	11:09:26.0
02461+6147	02:50:08.11	61:59:47.1	06337+1051	06:36:29.48	10:49:05.1	21074+4949	21:09:08.09	50:01:59.8
03233+5809**	03:27:22.33	58:19:45.8	06381+1039	06:40:58.00	10:36:48.8	21080+4950	21:09:42.83	50:08:29.5
03235+5808*	03:27:31.15	58:19:21.3	06412-0105*	06:43:44.97	-01:08:06.7	21202+5157*	21:21:53.18	52:10:43.6
04034+5107	04:07:11.93	51:24:44.7	06426+0025	06:45:15.50	00:22:25.9	21290+5535	21:30:38.70	55:48:59.6
04324+5102	04:36:16.08	51:08:12.8	06446+0029	06:47:12.87	00:26:06.5	21306+4927**	21:05:15.62	49:40:01.2
04324+5106*	04:36:19.70	51:12:44.6	06501+0143	06:52:45.57	01:40:14.9	21306+5540*	21:32:11.56	55:53:23.7
04366+5022*	04:40:26.12	50:28:24.7	06547-0109A	06:57:16.69	-01:13:39.5	21334+5039*	21:35:09.18	50:53:09.2
04547+4753*	04:58:29.66	47:58:27.6	06567-0355*	06:59:15.76	-03:59:39.0	21334+5329	21:35:05.86	53:43:01.2
04579+4703	05:01:39.74	47:07:23.1	06570-0401	06:59:30.95	-04:05:35.1	21407+5441*	21:42:23.68	54:55:06.7
05100+3723	05:13:25.43	37:27:04.5	07024-1102	07:04:45.65	-11:07:14.5	21413+5442*	21:43:01.36	54:56:16.3
05271+3059	05:30:21.22	31:01:27.2	07069-1045	07:04:45.65	-11:07:14.5	22134+5834*	22:15:09.08	58:49:09.3
05274+3345*	05:30:45.62	33:47:51.6	07061-0414*	07:08:38.75	-04:19:07.5	22308+5812*	22 32 46.01	58 28 21.8
05281+3412	05:31:26.60	34:14:57.7	07207-1435	07:23:01.28	-14:41:32.5	22475+5939*	22:49:29.47	59:54:56.6
05305+3029*	05:33:44.81	30:31:04.5	07295-1915**	07:33:10.45	-19:28:42.9	22502+5944**	22:51:59.86	59:59:16.9
05334+3149	05:36:41.08	31:51:13.8	07298-1919	07:32:02.46	-19:26:02.3	22506+5944*	22:52:38.63	60:00:55.8
05358+3543*	05:39:10.39	35:45:19.2	07299-1651*	07:32:10.00	-16:58:14.7	22539+5758	22:56:00.01	58:14:45.9
05361+3539	05:39:27.66	35:40:43.0	07333-1838	07:35:34.31	-18:45:32.5	22551+6139	22:57:11.23	61:56:03.4
05375+3536	05:40:52.52	35:38:23.8	07334-1842	07:35:40.95	-18:48:59.0	22570+5912*	22:59:06.50	59:28:27.7
05375+3540*	05:40:53.64	35:42:15.7	07422-2001	07:44:27.85	-20:08:31.9	23030+5958*	23:05:10.62	60:14:40.4
05490+2658	05:52:12.93	26:59:32.9	07427-2400*	07:44:51.90	-24:07:40.6	23033+5951	23:05:25.16	60:08:11.6
05480+2545*	05:51:10.75	25:46:14.3	07311-2204*	07:33:20.24	-22:10:57.7	23139+5939	23:16:09.32	59:55:22.8
05553+1631*	05:58:13.87	16:32:00.1	07434-2044	07:45:35.47	-20:51:38.6	23151+5912	23:17:21.09	59:28:48.8
						23545+6508**	23:57:05.23	65:25:10.8

\*Sources observed at 3.6 and 1.3 cm at high resolution.

\*\*Sources observed at 1.3 cm at high resolution.

<sup>a</sup>Source refereed as 18094-G12.20. Low resolution at 3.6 cm observation only. See text for details.<sup>b</sup>Source refereed as 19120-G45.47. Arguable designation: the IRAS source is more related with G45.45+0.06. Low resolution at 3.6 cm only. See text for details.

declination (J2000). These characteristics make the sources in the sample excellent candidates for identifying and studying HII regions, as well as for expanding the dataset of these objects to better understand their properties. Additional information about each source can be found in Appendix A.

We performed the data editing, calibration, and further mapping of all sample sources at 3.6 and 1.3 cm wavelengths following the standard techniques using the Common Astronomy Software Applications (CASA) of the NRAO version 5.3.0-143 (McMullin et al. 2007). The flux calibrator for observations at 3.6 and 1.3 cm was 3C48, and several

phase calibrators were used (see Table 3). 6 cm data were calibrated using the same procedure as was used for the 3.6 and 1.3 cm data. In order to obtain a similar angular resolution for continuum sources detected at two and three wavelengths, we convolved the data with the same beam. All observational parameters of the detected sources (position, flux density, and deconvolved angular size) were obtained with the task IMFIT of CASA.

From the subsample of 96 IRAS sources observed at 3.6 cm, we detect only 25 of them, while from the subsample of 52 sources observed at 1.3 cm, we detect only five. These five sources were also detected

TABLE 3  
PHASE CALIBRATOR'S OBSERVATIONAL PARAMETERS

Calibrator	RA (J2000) (h:m:s)	DEC (J2000) ( $^{\circ}$ : $'$ : $''$ )	3.6 Bootstrapped Flux Density (Jy)
2023+544	20h 23m 55.844s	54 $^{\circ}$ 27'35.83''	1.12 $\pm$ 0.01
2230+697	22h 30m 36.470s	69 $^{\circ}$ 46'28.08''	0.44 $\pm$ 0.01
0228+673	02h 28m 50.051s	67 $^{\circ}$ 21'03.03''	0.78 $\pm$ 0.02
0359+509	03h 59m 29.747s	50 $^{\circ}$ 57'50.16''	1.47 $\pm$ 0.03
0555+398	05h 55m 30.806s	39 $^{\circ}$ 48'49.17''	4.86 $\pm$ 0.08
0530+135	05h 30m 56.417s	13 $^{\circ}$ 31'55.15''	1.40 $\pm$ 0.02
0700+171	07h 00m 01.525s	17 $^{\circ}$ 09'21.70''	1.11 $\pm$ 0.01
0725-009	07h 25m 50.640s	00 $^{\circ}$ 54'56.54''	0.95 $\pm$ 0.01
0730-116	07h 30m 19.112s	-11 $^{\circ}$ 41'12.60''	4.63 $\pm$ 0.05
0828-375	08h 28m 04.780s	-37 $^{\circ}$ 31'06.28''	1.07 $\pm$ 0.01

TABLE 4  
SOURCES DETECTED AT 3.6 CM

IRAS <sup>a</sup> Source	VLA 3.6 cm Source	RA (J2000) (h:m:s)	Dec (J2000) ( $^{\circ}$ : $'$ : $''$ )	Distance <sup>b</sup> (kpc)	$L_{\text{FIR}}^{\text{b}}$ ( $10^4 L_{\odot}$ )
01045+6505	01045-VLA	01:07:51.34	65:21:22.4	10.7 <sup>1</sup>	8.00 <sup>17</sup>
01133+6434	01133-VLA	01:16:36.67	64:50:42.4	4.1 <sup>2</sup>	0.84 <sup>2</sup>
03235+5808	03235-VLA	03:27:31.34	58:19:21.7	4.2 <sup>2</sup>	1.30 <sup>2</sup>
04324+5106	04324-VLA	04:36:21.03	51:12:54.7	5.8 <sup>3</sup>	6.00 <sup>3</sup>
04366+5022	04366-VLA	04:40:27.20	50:28:29.2	5.9 <sup>3</sup>	3.00 <sup>3</sup>
05305+3029	05305-VLA	05:33:45.83	30:31:18.0	10.4 <sup>4</sup>	0.60 <sup>4</sup>
05358+3543	05358-VLA1	05:39:15.62	35:46:42.1	1.8 <sup>5</sup>	0.66 <sup>5</sup>
	05358-VLA2	05:39:15.13	35:46:41.6	1.8 <sup>5</sup>	0.66 <sup>5</sup>
05553+1631	05553-VLA	05:58:13.53	16:31:58.4	1.2 <sup>3</sup>	0.20 <sup>3</sup>
06055+2039	06055-VLA	06:08:35.44	20:39:03.5	2.9 <sup>3</sup>	3.00 <sup>3</sup>
06412-0105	06412-VLA	06:43:48.42	-01:08:20.5	7.1 <sup>3</sup>	9.00 <sup>3</sup>
06567-0355	06567-VLA	06:59:15.74	-03:59:36.8	2.3 <sup>6</sup>	1.80 <sup>18</sup>
07299-1651	07299-VLA	07:32:09.79	-16:58:12.2	1.4 <sup>3</sup>	0.70 <sup>3</sup>
07311-2204	07311-VLA	07:33:19.92	-22:10:57.5	8.0 <sup>7</sup>	20.00 <sup>7</sup>
07427-2400	07427-VLA	07:44:52.03	-24:07:42.1	6.9 <sup>3</sup>	50.10 <sup>19</sup>
07528-3441	07528-VLA	07:54:56.12	-34:49:37.8	1.2 <sup>8</sup>	20.00 <sup>8</sup>
08189-3602	08189-VLA	08:20:54.92	-36:13:02.5	7.6 <sup>3</sup>	30.00 <sup>20</sup>
18094-1823 <sup>c</sup>	18094-G12.20	18:12:23.63	-18:22:53.7	14.0 <sup>13</sup>	86.80 <sup>14</sup>
19120+1103 <sup>d</sup>	19120-G45.47	19:14:25.67	11:09:26.0	8.4 <sup>15</sup>	49.2 <sup>16</sup>
21306+5540	21306-VLA	21:32:11.76	55:53:40.9	3.7 <sup>9</sup>	1.10 <sup>3</sup>
21334+5039	21334-VLA	21:35:11.13	50:52:13.1	5.0 <sup>10</sup>	2.10 <sup>10</sup>
21413+5442	21413-VLA	21:43:01.47	54:56:18.0	7.9 <sup>11</sup>	1.45 <sup>11</sup>
22134+5834	22134-VLA	22:15:09.25	58:49:08.9	2.3 <sup>3</sup>	1.34 <sup>3</sup>
22308+5812	22308-VLA	22:32:45.62	58:28:18.2	5.7 <sup>3</sup>	9.00 <sup>3</sup>
23030+5958	23030-VLA	23:05:10.20	60:14:47.2	4.4 <sup>12</sup>	10.00 <sup>3</sup>

<sup>a</sup>The observed source does not necessary coincide with the IRAS source.

<sup>b</sup>The distance and the FIR luminosity are from the IRAS region, and do not necessary correspond to the observed sources at 3.6 cm. Values taken from: 1.- Rudolph De Geus & Wouterloot (1996), 2.- Maud et al. (2015), 3.- Wouterloot & Brand (1989), 4.- Lumsden et al. (2013), 5.- Lu et al. (2014), 6.- Tapia et al. (1997), 7.- May, Alvarez, & Bronfman (1997), 8.- Preite-Martínez (1988), 9.- Kim, Kim, & Kim (2015), 10.- McCutcheon et al. (1991), 11.- Navarrete et al. (2015), 12.- Lee, Murray, & Rahman (2012), 13.- Hill et al. (2005), 14.- We assume the IRAS FIR luminosity of G12.21-0.10 (de la Fuente et al. 2018, 2020a), 15.- Wu et al. (2019), 16.- We assume the IRAS FIR luminosity of G45.45+0.06 (de la Fuente et al. 2020a), 17.- Snell, Carpenter & Heyer (2002), 18.- Klein et al. (2005), 19.- MacLeod et al. (1998), 20.- Planck Collaboration et al. (2015).

<sup>c</sup>This source was not included in the original sample of 94 sources (see Table 3).

<sup>d</sup>This source was not included in the original sample of 94 sources (see Table 3). The nearest IRAS source is 19120+1103, but this coincides in position with the UC H II region with extended emission G45.455+0.058 or G45.45+0.06 (de la Fuente et al. 2020a). See text for discussion. The distance is adopted from Wu et al. (2019).

TABLE 5  
OBSERVATIONAL PARAMETERS OF THE SOURCES DETECTED AT 1.3, 3.6, AND 6.0 CM

VLA 3.6 cm Source	$\lambda$ (cm)	$S_\nu$ (mJy)	Beam Size ( " × " )	PA (deg)	RMS Noise (mJy beam <sup>-1</sup> )	Size ( " × " )
01045-VLA	6.0	140.4±4.2	1.57×1.05	134	0.25	3.13×2.91
—————	3.6	289.8±6.7	1.57×1.05	120	0.41	3.10×2.92
—————	1.3	100.5±5.4	1.57×1.05	27	0.67	3.12×3.00
01133-VLA	6.0	1.5±0.3	1.61×1.07	168	0.06	3.11×1.73
—————	3.6	2.1±0.1	1.61×1.07	129	0.06	1.75×1.15
03235-VLA	6.0	1.7±0.1	1.41×1.10	146	0.03	1.50×1.13
—————	3.6	6.6±0.2	1.41×1.10	144	0.07	1.48×1.16
04324-VLA	6.0	50.0±2.1	1.34×1.08	47	0.06	8.82×7.27
—————	3.6	97.7±3.3	1.34×1.08	46	0.12	8.85×8.31
04366-VLA	6.0	1.8±0.1	1.30×1.08	141	0.03	2.41×1.73
—————	3.6	5.0±0.4	1.30×1.08	158	0.03	2.72×2.27
05305-VLA	6.0	0.4±0.1	1.26×1.15	146	0.02	1.32×1.15
—————	3.6	0.21±0.01	1.26×1.15	120	0.02	1.30×1.21
05358-VLA1	3.6	1.8±0.2	0.88×0.74	139	0.02	3.04×1.05
05358-VLA2	3.6	0.8±0.1	0.88×0.74	30	0.02	2.35×1.49
05553-VLA	3.6	0.8±0.1	1.00×0.62	135	0.03	1.11×0.82
06055-VLA	3.6	0.8±0.1	1.11×0.74	124	0.09	1.30×0.82
06412-VLA	6.0	850.0±47.0	1.51×1.25	57	0.67	13.85×12.17
—————	3.6	685.0±48.0	1.51×1.25	62	0.90	12.97×10.74
—————	1.3	660.0±44.0	1.51×1.25	146	1.90	12.59×12.36
06567-VLA	6.0	49.3±3.2	1.69×1.24	161	0.21	4.58×3.65
—————	3.6	37.0±1.1	1.69×1.24	166	0.07	3.68×3.53
07299-VLA	3.6	0.26±0.01	1.40×0.76	148	0.01	1.44×0.86
07311-VLA	3.6	4.0±0.3	1.50×0.76	165	0.01	6.26×5.28
07427-VLA	3.6	2.3±0.2	1.65×0.77	160	0.02	1.81×0.95
07528-VLA	6.0	16.0±1.1	4.52×1.14	153	0.08	5.57×3.30
—————	3.6	17.4±1.3	4.52×1.14	163	0.12	6.08×2.85
08189-VLA	3.6	16.5±1.6	4.24×1.17	176	2.72	26.66×16.20
—————	1.3	18.2±1.8	4.24×1.17	179	2.45	19.43×10.77
18094-G12.20	3.6	7.2±0.1	12.54×7.26	167	0.15	12.84×7.31
19120-G45.47	3.6	112.4±1.7	8.23×7.64	159	1.34	8.34×7.63
21306-VLA	6.0	74.0±3.3	1.81×1.14	116	0.46	3.87×3.37
—————	3.6	39.9±2.6	1.81×1.14	128	0.40	3.35×2.76
21334-VLA	6.0	7.7±0.1	1.80×1.15	93	0.12	1.82×1.21
—————	3.6	5.7±0.1	1.80×1.15	93	0.06	1.84×1.17
21413-VLA	6.0	115.7±3.7	1.87×1.13	93	0.29	2.18×1.40
—————	3.6	177.1±4.4	1.87×1.13	91	0.73	2.13×1.32
—————	1.3	441.8±9.8	1.87×1.13	90	1.89	2.04×1.24
22134-VLA	3.6	4.7±0.3	0.82×0.72	116	0.20	0.98×0.84
22308-VLA	6.0	203.0±13.0	1.90×1.07	86	0.47	7.66×5.02
—————	3.6	433.0±25.0	1.90×1.07	79	1.14	7.67×5.07
23030-VLA	6.0	945.0±44.0	1.62×1.19	95	1.40	14.79×7.50
—————	3.6	1226.0±72.0	1.62×1.19	90	2.52	12.79×5.52
—————	1.3	1670.0±110.0	1.62×1.19	96	5.86	12.19×5.65

at 3.6 cm (see Table 4). The low detection rate may be due to the low sensitivity of the observations carried out in snapshot mode, but other reasons cannot be ruled out (see § 4.1).

Observational parameters of all detected IRAS sources at 1.3, 3.6, and 6 cm are listed in Table 5, and their respective radio contour maps are shown in Figures 1, 2, 3, and 4. Detailed results for each of the sources are provided in Appendix A.

### 3. RESULTS

#### 3.1. 3.6 cm Continuum Emission: Physical Parameters

In order to investigate the nature of the radio continuum sources detected toward the IRAS regions, we used the 3.6 cm flux density to determine their physical parameters as if they were optically thin H II regions at this wavelength. We also assumed an homogeneous and isothermal gas, with a spherically symmetric distribution, composed of

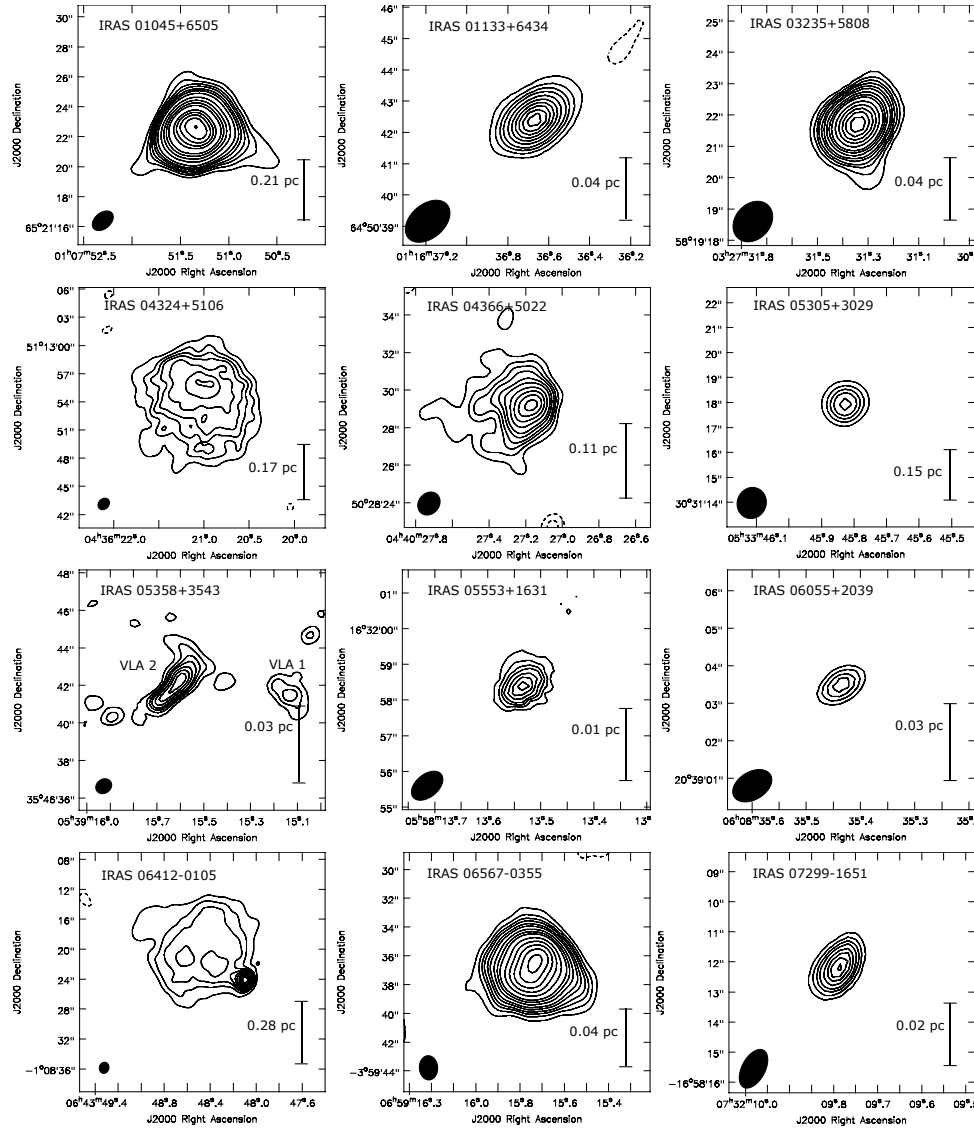


Fig. 1. Continuum contour maps of the sources detected at 3.6 cm. The contours for each source are: IRAS 01045+6505: -5, 5, 10, 15, 30, 60, 90, 120, 150, 180; IRAS 01133+6434: -5, -3, 3, 5, 7, 9, 12, 15, 18, 21, 24, 27; IRAS 03235+5808: -5, -3, 3, 5, 7, 9, 12, 15, 20, 25, 30, 40, 50, 60, 70, 80; IRAS 04324+5106: -5, -3, 3, 5, 7, 9, 12, 15, 18; IRAS 04366+5022: -5, -3, 3, 5, 7, 9, 12, 15, 20, 25, 30, 35; IRAS 05305+3029: -5, -3, 3, 5, 7, 9, 12, 15, 18; IRAS 05358+3543: -5, -3, 3, 5, 7, 9, 12, 15, 18; IRAS 05553+1631: -5, -3, 3, 5, 7, 9, 12, 15, 18; IRAS 06055+2039: -5, -3, 3, 4, 5, 6, 7; IRAS 06412-0105: -5, -3, 3, 5, 7, 9, 12, 15, 20, 25, 30; IRAS 06567-0355: -5, -3, 3, 5, 7, 9, 12, 15, 20, 25, 30, 40, 50, 60, 70, 80, and IRAS 07299-1651: -5, -3, 9, 12, 15, 18, 21 times the respective rms listed in Table 5. The beam size is shown at bottom left and given in Table 5.

pure hydrogen and a canonical value for the electronic temperature of  $10^4$  K. The electronic density ( $n_e$ ), emission measure ( $EM$ ), the mass of the ionized gas ( $M_{\text{HII}}$ ), and the total rate of Lyman continuum photons of the ionizing star ( $N'_c$ ) were calculated in the standard way using equations 1 to 4 (Schraml & Mezger 1969; Kurtz et al. 1994):

$$\left(\frac{n_e}{\text{cm}^{-3}}\right) = 7.8 \times 10^3 \left(\frac{\nu}{4.9 \text{ GHz}}\right)^{0.05} \left(\frac{S_\nu}{\text{mJy}}\right)^{0.5} \left(\frac{T_e}{10^4 \text{ K}}\right)^{0.175} \times \left(\frac{\theta_s}{\text{arcsec}}\right)^{-1.5} \left(\frac{D}{\text{kpc}}\right)^{-0.5}, \quad (1)$$

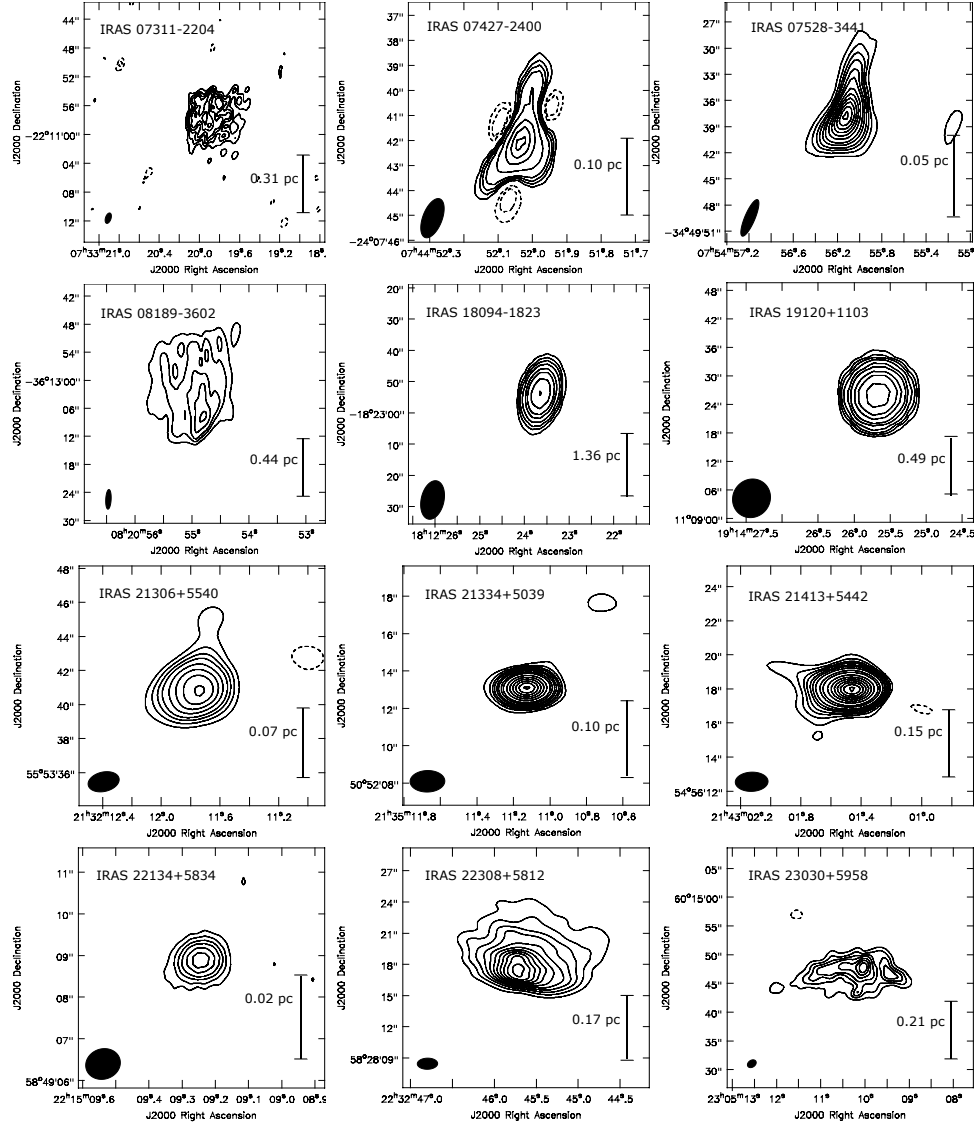


Fig. 2. Continuum contour maps of the sources detected at 3.6 cm. The contours for each source are: IRAS 07311-2204: -5, -3, 3, 5, 7, 9, 12, 15, 18; IRAS 07427-2400: -5, 5, 10, 20, 40, 60, 80; IRAS 07528-3441: -5, -3, 3, 5, 7, 9, 12, 15, 20, 25, 30, 35, 40, 45; IRAS 08189-3602: -4, -3, 3, 4, 5, 7, 9, 11, 13; IRAS 18094-1823: -5, -3, 3, 5, 7, 10, 15, 20, 30, 45; IRAS 19120+1103: -5, -3, 3, 5, 7, 10, 15, 20, 30, 40, 60, 80, 100, 150, 200, 250; IRAS 21306+5540: -5, -3, 3, 5, 7, 9, 12, 15, 18, 21; IRAS 21334+5039: -5, -3, 3, 5, 7, 9, 12, 15, 20, 25, 35, 45, 55, 65, 75, 85; IRAS 21413+5442: -5, -3, 3, 5, 7, 9, 12, 15, 20, 30, 40, 60, 80, 100, 120, 140, 160, 180; IRAS 22134+5834: -5, -3, 3, 5, 7, 9, 12, 15, 18; IRAS 22308+5812: -5, -3, 3, 5, 7, 9, 11, 13, 15, 17, 19, 21, 23, and IRAS 23030+5958: -5, -3, 3, 5, 7, 9, 12, 15, 18 times the respective rms listed in Table 5. The beam size is shown at bottom left and given in Table 5.

$$\left(\frac{EM}{\text{pc cm}^{-6}}\right) = 4.4 \times 10^5 \left(\frac{\nu}{4.9 \text{ GHz}}\right)^{0.1} \left(\frac{S_\nu}{\text{mJy}}\right) \left(\frac{T_e}{10^4 \text{ K}}\right)^{0.35} \times \left(\frac{\Theta_s}{\text{arcsec}}\right)^{-2}, \quad (2)$$

$$\left(\frac{M_{\text{HII}}}{M_\odot}\right) = 3.7 \times 10^{-5} \left(\frac{\nu}{4.9 \text{ GHz}}\right)^{0.05} \left(\frac{S_\nu}{\text{mJy}}\right)^{0.5} \left(\frac{T_e}{10^4 \text{ K}}\right)^{0.175} \times \left(\frac{\Theta_s}{\text{arcsec}}\right)^{1.5} \left(\frac{D}{\text{kpc}}\right)^{2.5}, \quad (3)$$

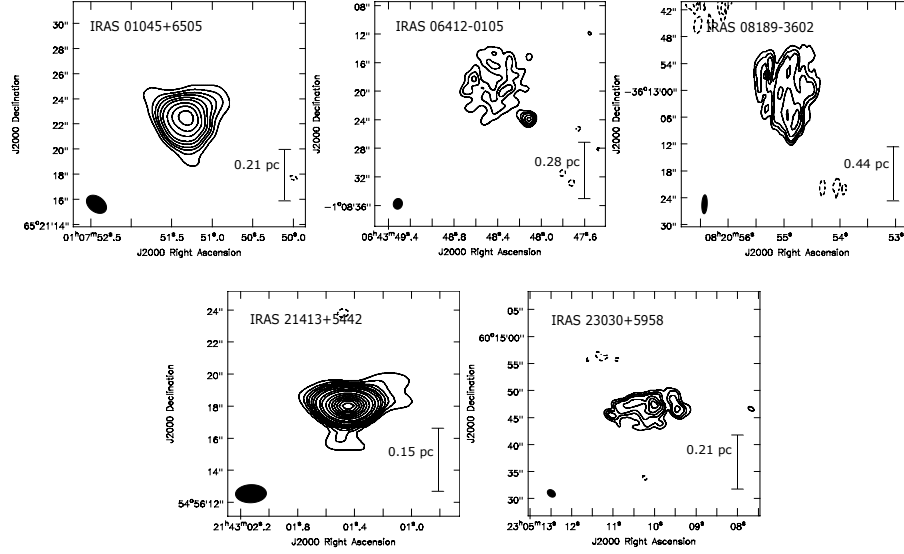


Fig. 3. Contour maps of the continuum emission from sources detected at 1.3 cm. The respective contour levels for each source are: IRAS 01045+6505: -5, -3, 3, 5, 10, 15, 20, 25, 30; IRAS 06412-0105: -4, -3, 3, 4, 5, 7, 9; IRAS 08189-3602: -4, -3, 3, 4, 5, 7, 9, 11; IRAS 21413+5442: -5, -3, 3, 5, 7, 9, 12, 15, 20, 30, 40, 60, 80, 100, 120, 140, 160, 180, and IRAS 23030+5958: -4, -3, 3, 4, 5, 7, 9, 11 times the respective rms reported in Table 5. The beam size is shown at bottom left and given in Table 5.

TABLE 6

## PHYSICAL PARAMETERS OF THE SOURCES USING THEIR 3.6 CM CONTINUUM EMISSION

VLA 3.6 cm Source	Size (pc)	$EM$ ( $10^6 \text{ cm}^{-6} \text{ pc}$ )	$n_e$ ( $10^3 \text{ cm}^{-3}$ )	$M_{\text{H II}}$ ( $M_{\odot}$ )	$N_i$ ( $\text{s}^{-1}$ )	Spectral Type	H II region <sup>a</sup> Type
01045-VLA	0.16	21.30	11.68	0.5792	48.39	O8	C
01133-VLA	0.03	0.67	4.80	0.0015	45.41	B1	UC
03235-VLA	0.03	2.54	9.72	0.0025	45.93	B0.5	UC
04324-VLA	0.24	0.88	1.91	0.3501	47.38	B0	C
04366-VLA	0.07	0.53	2.71	0.0129	46.10	B0.5	UC
05305-VLA	0.06	0.09	1.18	0.0039	45.22	B1	UC
05358-VLA1 <sup>b</sup>	0.02	0.29	4.03	0.0003	44.64	B2	UC
05358-VLA2	0.02	0.14	2.92	0.0002	44.27	B2	UC
05553-VLA	0.01	0.57	10.08	0.00002	43.93	B3	UC
06055-VLA	0.01	0.47	5.61	0.0002	44.69	B2	UC
06412-VLA	0.41	3.24	2.82	2.4979	48.40	O8	C
06567-VLA	0.04	1.89	6.85	0.0058	46.16	B0.5	UC
07299-VLA	0.01	0.13	4.10	0.00003	43.57	B3	UC
07311-VLA	0.22	0.08	0.60	0.0873	46.27	B0.5	C
07427-VLA	0.05	0.82	4.21	0.0054	45.91	B0.5	UC
07528-VLA	0.03	0.58	4.72	0.0011	45.26	B1	UC
08189-VLA	0.79	0.02	0.17	1.1159	46.84	B0	UC
18094-G12.20	0.68	0.05	0.26	1.0963	47.02	B0	UC
19120-G45.47	0.33	1.17	1.90	0.8519	47.76	O9.5	C
21306-VLA	0.05	2.84	7.19	0.0155	46.60	B0.5	UC
21334-VLA	0.04	1.66	6.74	0.0043	46.02	B0.5	UC
21413-VLA	0.07	39.41	24.39	0.0924	47.91	O9.5	UC
22134-VLA	0.01	3.78	19.30	0.0003	45.26	B1	UC
22308-VLA	0.18	7.10	6.35	0.4514	48.01	O9	C
23030-VLA	0.20	9.73	7.06	0.6858	48.24	O8.5	C

<sup>a</sup>UC = UC H II region and C = Compact H II region.

<sup>b</sup>This source has an elongated, jet-like morphology. See Appendix A.

$$\left(\frac{N'_e}{\text{s}^{-1}}\right) \geq 8.04 \times 10^{46} \left(\frac{T_e}{\text{K}}\right)^{-0.85} \left(\frac{r}{\text{pc}}\right)^3 \left(\frac{n_e}{\text{cm}^{-3}}\right)^2. \quad (4)$$

where  $\nu$  is the frequency,  $S_\nu$  the flux density,  $T_e$  the electronic temperature,  $D$  the distance,  $r$  is the radius of the sphere, and  $\Theta_s$  is its size. The distance

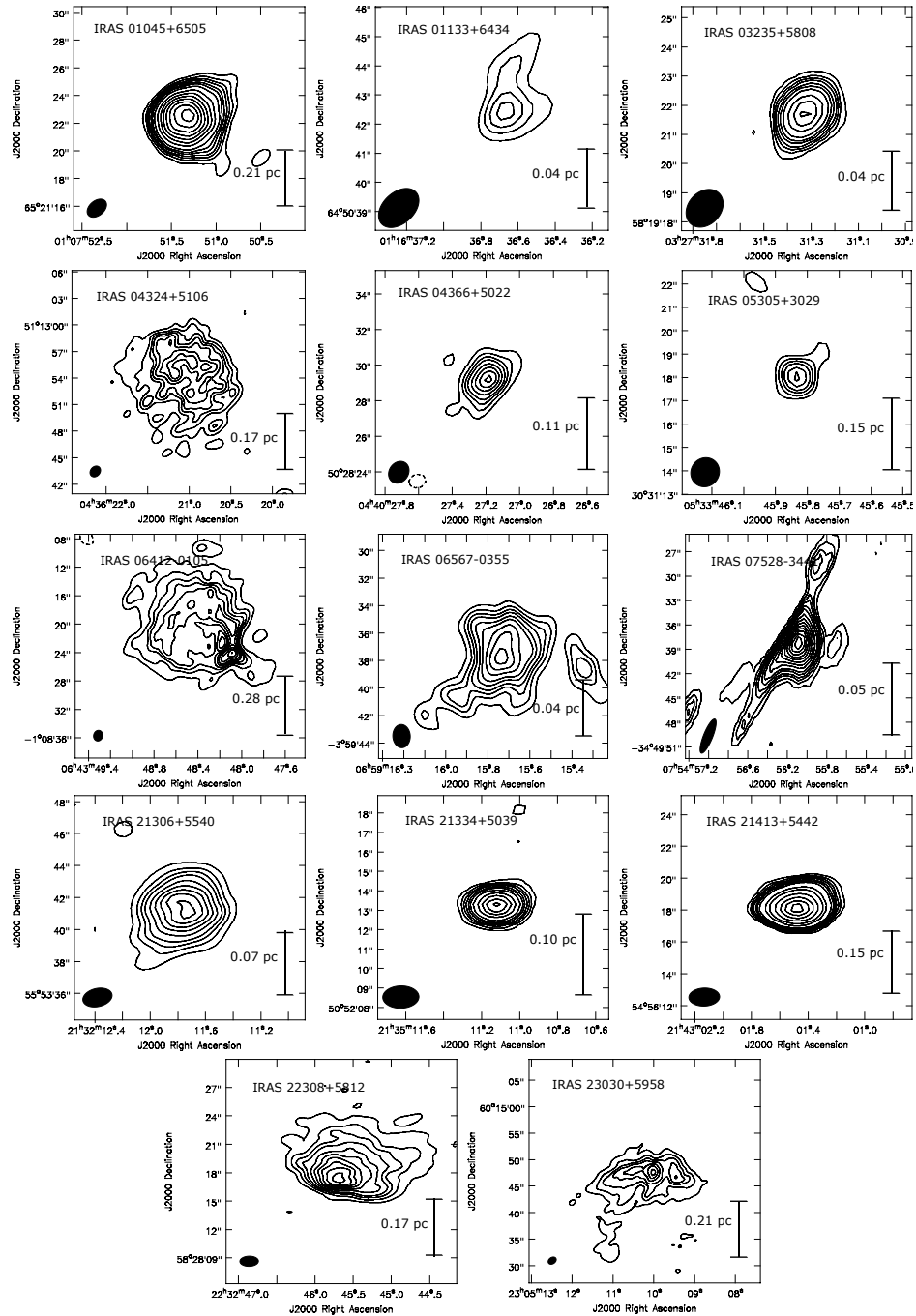


Fig. 4. Continuum contour maps of the sources with 6 cm emission (these observations have been reported previously by Urquhart et al. (2009); see § 2). The contours for each source are: Continuum contour maps of the sources detected at 6.0 cm. The contours for each source are: IRAS 01045+6505: 5, 10, 15, 20, 40, 60, 100, 140, 200; IRAS 01133+6434: -5, -3, 3, 5, 7, 9, 12, 15, 18; IRAS 03235+5808: -5, -3, 3, 5, 7, 9, 12, 15, 20, 30, 40, 50; IRAS 04324+5106: -5, -3, 3, 5, 7, 9, 12, 15, 18; IRAS 04366+5022: -5, -3, 3, 5, 7, 9, 12, 15, 18, 21; IRAS 05305+3029: -3, 3, 5, 7, 9, 12, 15, 18; IRAS 06412-0105: -5, -3, 3, 5, 7, 9, 12, 15, 20, 25, 30; IRAS 06567-0355: -5, -3, 3, 5, 7, 9, 12, 15, 20, 25, 30; IRAS 07528-3441: -5, -3, 3, 5, 7, 9, 12, 15, 20, 25, 30, 35, 40, 45, 50, 55; IRAS 21306+5540: -5, -3, 3, 5, 7, 9, 12, 15, 18, 21, 24; IRAS 21334+5039: -5, -3, 3, 5, 7, 9, 12, 15, 20, 30, 40, 50, 60; IRAS 21413+5442: -5, -3, 3, 5, 7, 9, 12, 15, 20, 40, 60, 100, 150, 200, 250; IRAS 22308+5812: -5, -3, 3, 5, 7, 9, 12, 15, 18, 21, 24, 27, and IRAS 23030+5958: -5, -3, 3, 5, 7, 9, 12, 15, 18 times the respective rms listed in Table 5. The beam size is shown at bottom left and given in Table 5.

and flux density values at 3.6 cm for all continuum sources were taken from Tables 4 and 5, respectively, and the size of the sources was calculated using the mean of their two axes. In addition, the ionizing spectral type was determined following Panagia (1973), considering zero-age main-sequence (ZAMS) objects.

The physical parameters calculated from the 3.6 cm flux density are listed in Table 6. Most of the calculated parameters for the continuum sources meet the definition of the UC H II region according to Wood & Churchwell (1989); Kurtz et al. (1994). Although the determination of the physical parameters using the flux density at 3.6 cm is an acceptable approximation, a better characterization requires observations in at least two wavelengths to estimate their spectral index. For this reason, caution must be taken when interpreting these results.

### 3.2. Spectral Indices

The spectral index provides more reliable information about the nature of the sources. However, to calculate it requires that the sources are detected in at least two wavelengths. The spectral index,  $\alpha$  is calculated using a power-law function  $S_\nu \propto \nu^\alpha$  (being  $S$  the flux density at the frequency  $\nu$ ), and its value indicates whether the continuum emission is thermal or non-thermal in nature. For example, at centimeter wavelengths, optically thin H II regions are associated with a spectral index around  $-0.1$ , while optically thick H II regions have an index  $\approx 2$  (e.g. Trinidad et al. 2003). Thermal jets, on the other hand, have a spectral index of approximately 0.6 (e.g. Anglada, Rodríguez, & Carrasco-González 2018, and references therein). In contrast, the active magnetosphere of some young low-mass stars has a spectral index ranging from  $-2$  to  $2$  (e.g. Rodríguez et al. 2012), while starburst galaxies have a spectral index ranging from  $-1.2$  to  $-0.4$  (e.g. Deeg et al. 1993). Furthermore, the spectral index allows to infer the degree of optical depth of the emission. In the case of thermal emission, its value, together with the morphology, could indicate whether the source is consistent with an H II region or a thermal jet.

As mentioned, only five sources in the sample were detected at both 3.6 and 1.3 cm. To increase the number of characterized sources, we also used observations at 6 cm from 14 sources reported by Urquhart et al. (2009). Out of the 25 sources listed in Table 5, 14 were found to have emission at 3.6 and 6 cm, while only one source showed emission at both 1.3 and 3.6 cm and four sources were detected at 1.3, 3.6, and 6 cm.

TABLE 7  
SPECTRAL INDEX OF THE SOURCES  
DETECTED\*

VLA 3.6 cm Source	Wavelength (cm)	Spectral Index
01045-VLA	3.6 & 6	$1.3 \pm 0.2$
01133-VLA	3.6 & 6	$0.6 \pm 0.8$
03235-VLA	3.6 & 6	$2.4 \pm 0.2$
04324-VLA	3.6 & 6	$1.2 \pm 0.2$
04366-VLA	3.6 & 6	$1.9 \pm 0.5$
05305-VLA	3.6 & 6	$-1.2 \pm 0.5$
06412-VLA	1.3, 3.6 & 6	$-0.2 \pm 0.4$
06567-VLA	3.6 & 6	$-0.5 \pm 0.3$
07528-VLA	3.6 & 6	$0.2 \pm 0.4$
08189-VLA	1.3 & 3.6	$0.1 \pm 0.3$
21306-VLA	3.6 & 6	$-1.1 \pm 0.3$
21334-VLA	3.6 & 6	$-0.6 \pm 0.1$
21413-VLA	1.3, 3.6 & 6	$0.9 \pm 0.2$
22308-VLA	3.6 & 6	$1.4 \pm 0.4$
23030-VLA	1.3, 3.6 & 6	$0.4 \pm 0.3$

\* At two and/or three wavelengths.

Because of the 1.3 and 3.6 cm observations have a similar  $(u,v)$  coverage and were carried out using the same calibrators with a time difference of about 4.5 months, assuming that their flux density had no significant variations over time, we can estimate a reliable spectral index for the continuum sources detected at these two wavelengths. Although 6 cm observations were carried out over a decade later and with slightly lower angular resolution than those at 1.3 and 3.6 cm, they can still be used to estimate a rough spectral index. As mentioned in § 2, all data were convolved to have a similar angular resolution (see Table 5). The calculated spectral indices are reported in Table 7.

Based on spectral indices and morphology (size, shape, and internal structure, mainly at 3.6 cm), we confirm that the majority of continuum sources could be consistent with H II regions, five of them associated with optically thick emission, three with optically thin emission, and three with partially optically thin emission. Additionally, we identified four continuum sources with a negative spectral index, which indicates non-thermal emission.

### 3.3. H II Region Models

In general, the physical parameters of H II regions are calculated assuming a homogeneous electron density. However, models that account for specific density distributions, such as the outwardly decreasing density model, are expected to provide a more reliable understanding of the ionized gas physics than the ideal Stromgren sphere model, which does not consider these gradients. One of such model was developed by Olnon (1975).

Olson's models assume ionized hydrogen gas, circular symmetry for the radius perpendicular along the line of sight, and uniform electron temperature ( $T_e$ ). In the Rayleigh-Jeans regime, the total flux density is given by

$$S_\nu = \frac{4\pi k T_e \nu^2}{c^2 D^2} \int_0^\infty \rho \left[1 - e^{-\tau_\nu(\rho)}\right] d\rho,$$

where  $\rho$  is the radius perpendicular to the line of sight and  $D$  is the distance to the object.

The optical depth is defined as:

$$\tau_\nu(\rho) = f(\nu, T_e) E(\rho) = 8.235 \times 10^{-2} T_e^{-1.35} \nu^{-2.1} E(\rho).$$

The emission measure can be expressed as

$$E(\rho) = 2 \int_0^\infty n_e^2(r) dz,$$

where  $r^2 = \rho^2 + z^2$  and the distance along the line of sight is  $z$ . With this background and following Olson (1975), we explored models with cylindrical, spherical, and Gaussian distributions.

For the *cylindrical distribution*, we considered a cylinder with radius= $R$  and length= $2R$ , where the electron density  $n_e$  is constant inside, and zero outside. Therefore:

$$S_\nu = \frac{2\pi k T_e R^2 \nu^2}{c^2 D^2} \left(1 - e^{-\tau'}\right). \quad (5)$$

In a similar way, the *spherical distribution* is given by

$$S_\nu = \frac{2\pi k T_e R^2 \nu^2}{c^2 D^2} \left[1 - \frac{2}{\tau'^2} [1 - (\tau' - 1)e^{-\tau'}]\right], \quad (6)$$

while the *Gaussian distribution* is defined by

$$S_\nu = \frac{2\pi k T_e R^2 \nu^2}{c^2 D^2} [\gamma + \ln \tau'' + E_1(\tau'')], \quad (7)$$

where the H II region has spherical symmetry, but the electron density distribution is not constant; there is a density gradient with a Gaussian distribution.

In these equations,  $R$  is the source radius,  $D$  is the distance,  $\tau' = 2n_0^2 R f$ ,  $\tau'' = n_0^2 R f \sqrt{\pi}$ ,  $\gamma$  is Euler's constant, and  $E_1(\tau)$  is the exponential integral, defined as  $E_1(x) \equiv \int_x^\infty (\exp^{-t}/t) dt$ . We used the least-squares fit method in all these models to find

the best values for the radius and density using the minimizing function in Python software. We have

$$\chi^2 = \sum_i^N \frac{[S_{\nu_i}^{obs} - S_{\nu_i}^{mod}(a)]^2}{\epsilon_i^2}, \quad (8)$$

where  $S_{\nu_i}^{obs}$  is the set of observed data,  $S_{\nu_i}^{mod}$  is the model,  $a$  is the set of parameters in the model to be optimized in the fit,  $\epsilon_i$  is the estimated uncertainty in the flux density equal to  $(SN/2)(0.15S_{\nu_i}^{obs})$ , where  $SN$  is the signal to noise ratio.

#### 4. DISCUSSION

We employed the Olson models with cylindrical, spherical, and Gaussian distribution to confirm the nature of the H II regions suggested by the morphology (see Figures 1 and 2), 3.6 cm continuum emission (Table 5), and spectral indices (Table 7) for sources detected at two and three wavelengths. The first two models assume a homogeneous electron density, while the third model uses a density gradient with a Gaussian distribution. For sources detected at two or three bands, we obtained physical parameters using H II region models with cylindrical (equation 5), spherical (equation 6), and Gaussian (equation 7) geometries.

Assuming an isothermal ionized gas with a temperature of  $10^4$  K, we minimized equation 8 to obtain the best spectral fit for each source. H II region models were applied to 11 sources from Table 7 with a spectral index greater than  $\approx -0.1$ . Of these, eight were detected at two wavelengths, and three were detected at three wavelengths. The resulting best fits for each source are shown in Figure 5, and their respective physical parameters, as determined by the best fit, are listed in Table 8. However, from our two or three wavelength dataset, we were unable to accurately discriminate between specific models for the symmetry and structure of H II regions, highlighting the need for additional multi-band observations. In this way, elements such as morphology and inferred substructure from observations can help us to characterize H II regions more accurately. For more details on each source, please refer to Appendix A.

We present the results in the form of a final catalog, (see Table 9), that summarizes the calculated physical parameters for 20 sources. These were calculated from 3.6 cm emission for sources detected at a single wavelength and from H II models for sources with two or three observations. Of these sources, 17 show physical parameters consistent with those typical of ultracompact H II regions (one with cometary morphology) and 3 are compatible with being compact H II regions. Of the remaining five sources listed

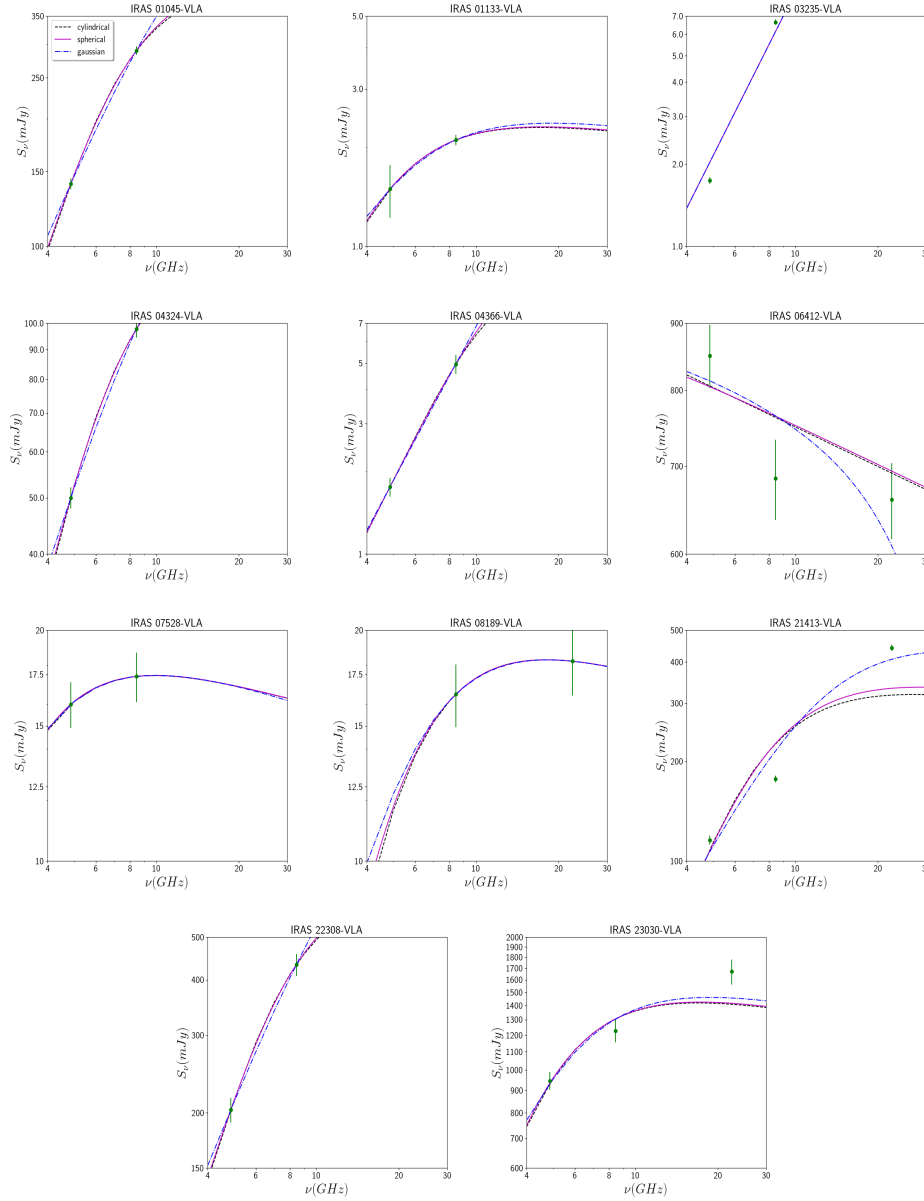


Fig. 5. Fits of the three models of the IRAS sources detected at two or three wavelengths. Dots are the observational data. Dash, continuous, and dash-dot lines are for cylindrical, spherical and Gaussian models, respectively. See the text for details.

in Table 6, 05358-VLA1 has an elongated jet-like morphology, while 05305-VLA, 06567-VLA, 21306-VLA, and 21334-VLA have a negative spectral index ( $< -0.5$ ).

#### 4.1. Detection Rate of H II Regions in the Sample

As mentioned, the sample consists of 106 IRAS sources, 96 of which were observed at 3.6 cm and 52 at 1.3 cm, with 42 of them observed at both wavelengths. The detection rate at 3.6 cm was  $\approx 25\%$

(25 sources), while at 1.3 cm it was only around 10% (five sources). There are several reasons that could account for this low detection rate, which will be explored below.

One possible reason for the low detection rate could be the poor sensitivity of the observations, which were made in snapshot mode, with integration times of 5 and 10 minutes at 3.6 and 1.3 cm, respectively. However, even with these integration

TABLE 8  
PHYSICAL PARAMETERS: H II REGION MODELS

VLA 3.6 cm Source	Size <sup>a</sup> (pc)	EM cm <sup>-6</sup> pc	$n_e$ cm <sup>-3</sup>	$N_i$ (s <sup>-1</sup> )	Spectral Type	Morphology	H II <sup>b</sup> Type
01045-VLA	0.16	$4.39 \times 10^8$	$8.92 \times 10^4$	$6.25 \times 10^{48}$	O6.5	Spherical	UC
01133-VLA	0.03	$1.60 \times 10^8$	$2.51 \times 10^5$	$4.80 \times 10^{45}$	B1	Spherical	UC
03235-VLA	0.03	$6.68 \times 10^9$	$1.63 \times 10^6$	$1.97 \times 10^{47}$	B0	Spherical	UC
04324-VLA	0.24	$4.67 \times 10^8$	$3.87 \times 10^5$	$6.11 \times 10^{47}$	O9.5	Gaussian	C
04366-VLA	0.07	$1.37 \times 10^9$	$6.41 \times 10^5$	$7.06 \times 10^{46}$	B0	Spherical	UC
06412-VLA	0.41	$1.19 \times 10^6$	$2.88 \times 10^3$	$3.26 \times 10^{48}$	O7.5	Gaussian	UC <sup>c</sup>
07528-VLA	0.03	$3.59 \times 10^7$	$1.02 \times 10^5$	$1.96 \times 10^{45}$	B1	Cylindrical	UC
08189-VLA	0.79	$1.71 \times 10^8$	$1.16 \times 10^5$	$1.30 \times 10^{47}$	B0	Spherical	UC
21413-VLA	0.07	$5.75 \times 10^8$	$3.10 \times 10^5$	$2.76 \times 10^{48}$	O8	Gaussian	UC
22308-VLA	0.18	$9.14 \times 10^8$	$4.04 \times 10^5$	$3.85 \times 10^{48}$	O7.5	Gaussian	UC
23030-VLA	0.20	$1.07 \times 10^8$	$8.85 \times 10^4$	$2.67 \times 10^{48}$	O8	Gaussian	UC

<sup>a</sup>Taken from the 3.6 cm RC emission.

<sup>b</sup> UC = UC H II region and C = Compact H II region.

<sup>c</sup> UC with cometary morphology.

TABLE 9  
FINAL CATALOG OF H II REGIONS<sup>a</sup>

IRAS Source	VLA 3.6 cm Source	Size (arcsec)	Size (pc)	EM (10 <sup>6</sup> cm <sup>-6</sup> pc)	$n_e$ (10 <sup>3</sup> cm <sup>-3</sup> )	$M_{\text{H II}}$ (M <sub>⊙</sub> )	H II <sup>a</sup> Type
01045+6505	01045-VLA	3.02	0.16	21.30	11.68	0.5792	UC
01133+6434	01133-VLA	0.83	0.03	0.67	4.80	0.0015	UC
03235+5808	03235-VLA	0.87	0.03	2.54	9.72	0.0025	UC
04324+5106	04324-VLA	8.56	0.24	0.88	1.91	0.3501	C
04366+5022	04366-VLA	2.30	0.07	0.53	2.71	0.0129	UC
05358+3543	05358-VLA2	1.84	0.02	0.14	2.92	0.0003	UC
05553+1631	05553-VLA	0.95	0.01	0.57	10.08	0.00002	UC
06055+2039	06055-VLA	0.95	0.01	0.47	5.61	0.0002	UC
06412-0105	06412-VLA	0.41	3.24	1.19	2.82	2.4979	UC <sup>b</sup>
07299-1651	07299-VLA	1.11	0.01	0.13	4.10	0.00003	UC
07311-2204	07311-VLA	5.75	0.22	0.08	0.60	0.0873	C
07427-2400	07427-VLA	1.31	0.05	0.82	4.21	0.0054	UC
07528-3441	07528-VLA	3.78	0.03	0.58	4.72	0.0011	UC
08189-3602	08189-VLA	3.48	0.79	0.02	0.17	1.1159	UC
18094-1823	18094-G12.20	2.10	0.68	0.05	0.26	1.0963	UC
19120-1103	19120-G45.47	2.20	0.33	1.17	1.90	0.8519	C
21413+5442	21413-VLA	1.70	0.07	39.41	24.39	0.0924	UC
22134+5834	22134-VLA	0.91	0.01	3.78	19.30	0.0003	UC
22308+5812	22308-VLA	6.24	0.18	7.10	6.35	0.4514	UC
23030+5958	23030-VLA	4.30	0.20	9.73	7.06	0.6858	UC

<sup>a</sup> UC = UC H II region and C = Compact H II region.

<sup>b</sup> UC with cometary morphology.

times, sources with a flux density of  $\approx 2$  mJy at 3.6 cm and  $\approx 4$  mJy at 1.3 cm could still be detected at  $3\sigma$ . Thus, this factor can only account for a few cases of non-detection. On the other hand, it is also known that the lifetime of the H II regions is relatively short, which could also contribute to the low detection rate.

We cannot rule out the possibility that the emission measure of potential H II regions is very large ( $> 10^9$  pc cm<sup>-6</sup>), making it optically thick at centimeter/millimeter wavelengths and resulting in a turnover frequency for optically thin emission of around 30 GHz or higher (Kurtz et al. 1994). This

would mean that they cannot be detected at 3.6 cm or even at 1.3 cm. On the other hand, Sewilo et al. (2011) observed a small sample of UC and HC H II region candidates at several bands and achieved a successful detection rate with flux density ranging from 60 to 350 mJy at 1.3 and 3.6 cm, respectively. Their sources span a range of distances up to 14.0 kpc, which is close to the upper end of the range of distances in our sample. However, the large sample of sources we have explored may include some objects, especially the most compact ones, that could be affected by opacity and become undetectable, particularly in the 6 cm band. Nonetheless, as shown

by Sewilo et al. (2011), this effect is not dominant, at least for the majority of H II regions observed at wavelengths above a few cm.

#### 4.2. Non-thermal Emission

In general, the nature of emission from astronomical sources can be classified as thermal (e.g. Olmon 1975; Reynolds 1986) and non-thermal (e.g. Deeg et al. 1993), if the spectral indices are larger than  $-0.1$  or less than  $-0.5$ , respectively. We explore some scenarios that could explain the nature of the continuum sources with a negative spectral index.

Negative spectral indices were found in four continuum sources (05305-VLA, 06567-VLA, 21306-VLA, and 21334-VLA), with values ranging from  $-1.3$  to  $-0.5$ , which indicate non-thermal emission. Young sources with spectral indices between  $-0.5$  and  $-0.1$  have been associated to gyro-synchrotron radiation, produced in strong collisions in radio jets (e.g. Trinidad, Rodríguez, & Rodríguez 2009) or in the corona of young low-mass stars (e.g. Launhardt et al. 2022). Since the sample sources are related to massive star formation regions, the first scenario could be the most likely; however, strong collisions are not expected in H II regions. Spectral indices as low as  $-1.2 < \alpha < -0.4$  are typically only found in starburst galaxies (e.g. Deeg et al. 1993).

The variability of continuum sources could also explain these negative values of the spectral index, since the observations at 3.6 and 6 cm were carried out about a decade apart. Another possibility is that the spectral index of these sources could be a result of the emission produced by two or more continuous sources. For example, for the sources IRAS 06567-VLA and IRAS 21306-VLA, there is marginal evidence that the continuous emission is not associated with a single source. In either case, to investigate the nature of these sources, new observations with higher sensitivity and angular resolution at multiple wavelengths are needed.

### 5. CONCLUSIONS

The UC H II regions are good tracers for places where early-type massive stars form; thus their study and characterization can provide important insights to understand the formation process of high-mass stars. However, due to their short lifetime, the number of known UC H II regions is relatively small. In this context, this paper is intended to increase the number of known H II regions (mainly ultra-compact) and to provide the basic data that can be used for further detailed investigations.

We conducted a study on the 1.3 and 3.6 cm continuum emission from a sample of 106 high-luminosity IRAS sources observed with the VLA in its C and B configuration, respectively. 52 sources of the sample were observed at 1.3 cm and 96 at 3.6 cm, with 42 of them observed at both wavelengths. Additionally, we used 6 cm observations reported in the literature for the detected sources. From the 3.6 cm observations, we detected 25 sources, while only 5 sources were detected from the 1.3 cm observations. In general, a single radio continuum source was detected toward each IRAS region, although there is marginal evidence of double systems in some regions. We only detected two independent sources in one region.

Using the 3.6 cm emission, we performed an initial characterization of the ionized gas in all detected sources by calculating their traditional physical parameters. For sources that were also detected at 1.3 cm and for those with reported 6 cm emission, we determined the spectral index and calculated models of H II regions with cylindrical, spherical, and Gaussian morphologies. Based on these results, we present a catalog of candidate H II regions detected in the sample.

## APPENDIX

### A. COMMENTS ON INDIVIDUAL SOURCES

General information is given below for the 25 sources detected at 3.6 cm, as well as the most relevant results of the study carried out in this paper. Table 4 lists the luminosity and distance for all sources, while Table 6 gives the physical parameters calculated from the 3.6 cm emission. In addition, Figures 1 and 2 display the 3.6 cm contour maps, and Figure 3 shows the 1.3 cm contour maps of the detected sources in the sample. Contour maps of sources with 6 cm emission are shown in Figure 4. The physical parameters obtained from the models of the H II regions with cylindrical, spherical and Gaussian symmetry, as well as the best fits to the observational data are given in Table 8 and Figure 5, respectively.

**IRAS 01045+6505** is located in the HCS 6236 molecular cloud (Snell, Carpenter & Heyer 2002). An UC H II region, spatially coincident with a CS molecular clump, and two submillimeter sources have been detected toward it (Mookerjea, Sandell & Wouterloot 2007). We detect 1.3 and 3.6 cm continuum emission toward IRAS 01045+6505. In the field, we observe only one compact source, which is also detected at 6 cm and coincides with the millimeter source 01045-SMM1 and the UC H II region re-

ported by Mookerjea, Sandell & Wouterloot (2007). A spectral index,  $\alpha \approx 0.3$  is estimated using the flux density of the three wavelengths. However, the flux density at 1.3 cm appears to be very low compared to those obtained at 3.6 and 6 cm, which makes the estimated spectral index unreliable. It is possible that the flux density of the source is variable with the time.

Using only the 3.6 and 6 cm flux densities, we estimated a value of  $\alpha \approx 1.3$ . We interpret this spectral index as an optically partially thick UC H II region, which is consistent with the interpretation given by Mookerjea, Sandell & Wouterloot (2007). No significant variations are observed in Figure 5 between the cylindrical, spherical and Gaussian geometries of the UC H II region; however, based on its morphology at 1.3 and 3.6 cm, the spherical model could be the most suitable.

**IRAS 01133+6434.** It was previously observed in radio continuum by Urquhart et al. (2009), finding only one radio source. In our study, we detected a single compact and spherical source in the field at 3.6 cm. However, at 6 cm, this continuum source exhibits two emission peaks, with the strongest one coinciding with the 3.6 cm emission. Using its 3.6 and 6 cm flux density, we estimated a spectral index of  $\approx 0.6$ , which is consistent with an optically partially thin H II region. The physical parameters obtained from the H II region models are given in Table 8, suggesting that it is an UC H II region sustained by a ZAMS B1 star. We did not find significant differences between the three models applied.

**IRAS 03235+5808.** This source has been little studied. Urquhart et al. (2009) detected a continuum source and  $\text{NH}_3$  emission in the region. A continuum source was detected at 3.6 and 6 cm, which has a compact and spherical morphology at both wavelengths and coincides spatially with the IRAS center position. Its spectral index ( $\alpha \approx 2.4$ ) and physical parameters suggest that it could be an optically thick UC H II region, which is confirmed by analyzing the H II region with three symmetries. The central source of the UC H II region is a ZAMS B0 star.

**IRAS 04324+5106.** A radio continuum source and four millimeter sources were detected in the region by Urquhart et al. (2009) and Klein et al. (2005), respectively. We observed a continuum source at 3.6 cm, that is very extended and shows a cometary morphology. This source is also detected at 6 cm with a similar morphology. Based on its spectral index between 3.6 and 6 cm (1.2) and applying the H II region models, we find that the contin-

uum source is consistent with a compact H II region with Gaussian symmetry (see Figure 5 and Table 8), which is associated with a ZAMS O9.5 star.

**IRAS 04366+5022.** Urquhart et al. (2009) detected a single continuum source at 6 cm, which has  $\text{NH}_3$  emission (Urquhart et al. 2011). We detected a continuum source toward IRAS 04366+5022 at wavelengths of 3.6 and 6 cm. This source, at 3.6 cm, shows an irregular morphology with several protuberances, suggesting the presence of more than one embedded continuum source (Figure 1). However, high angular resolution observations will be necessary to confirm this speculation.

Assuming that the continuum emission is produced by a single source, we estimated a spectral index of  $\approx 1.9$ . This value could be consistent with an optically thick H II region. Based on the H II region models, we found that its physical parameters are consistent with this assumption (see Figure 5 and Table 8).

**IRAS 05305+3029.** This source has been poorly studied and no ammonia or other molecular tracer has been detected in the region. A compact continuum source was detected in the field at 3.6 cm, located about  $14.3''$  northeast of the IRAS position. Although it was not detected at 1.3 cm, the continuum source was detected at 6 cm. It shows a compact morphology at 3.6 cm with a protuberance observed at 6 cm, suggesting that the continuum source could be a binary system. More sensitive observations will be necessary to verify this hypothesis.

We calculated a spectral index of  $\approx -1.2$ , which is too negative to be credible. This value could be explained by invoking variability of the continuum source and/or the possibility that it could be a double system. The physical parameters of this continuum source, using its 3.6 cm emission, are consistent with an UC H II region harboring a ZAMS B1 star. However, simultaneous multi-wavelength observations with high angular resolutions are necessary to confirm its nature.

**IRAS 05358+3543** is located toward the star cluster S233 (Yao et al. 2000) and has been studied at several wavelengths. Although it is strong at millimeter wavelengths (Beuther et al. 2002a), centimeter continuum emission has not been detected (e.g Sridharan et al. 2002). In addition, a massive bipolar outflow with a high degree of collimation has been detected (Beuther et al. 2002b).

The 3.6 cm continuum map reveals two sources in the field. The strongest source, IRAS 05358-VLA1, shows an elongated morphology in the northwest-southeast direction, while the second

source, IRAS 05358-VLA2, is weaker and more compact. Although IRAS 05358-VLA1 has a jet-like morphology, it was not detected at 1.3 cm nor at 6 cm; hence, its spectral index was not calculated. Moreover, this continuum source is not associated with the millimeter source detected by Beuther et al. (2002a) or the bipolar SiO outflow detected by Beuther et al. (2002b), whose center is about  $75''$  to the southeast. Nonetheless, the elongation of the IRAS 05358-VLA1 is similar to that of the SiO bipolar outflow (northwest-southeast direction). Although IRAS 05358-VLA1 does not seem to be the driver source of the SiO outflow, there may be some relationship. Furthermore, using its 3.6 cm emission, we estimated a mass-loss rate of  $\dot{M} = 2.71 \times 10^{-10} M_{\odot} \text{ yr}^{-1}$ , and a momentum rate of  $\dot{P} = 1.35 \times 10^{-7} M_{\odot} \text{ yr}^{-1} \text{ km s}^{-1}$ , suggesting this source is a thermal jet (e.g. Anglada, Rodríguez, & Carrasco-González 2018).

On the other hand, the derived physical parameters of the weak continuum source, IRAS 05358-VLA2, seem to be consistent with an UC H II region hosting a ZAMS B2 star.

**IRAS 05553+1631** is one of the nearest regions in the sample ( $\approx 1.2$  kpc; (Wouterloot & Brand 1989)). A millimeter source was detected by Williams, Fuller, & Sridharan (2004) in the region. We detected one compact and spherical continuum source at 3.6 cm, which is offset by approximately  $\approx 2.5''$  from the millimeter source. Based on its physical parameters, we suggest that it could be an UC H II region, harboring a ZAMS B3 star.

**IRAS 06055+2039** is located toward S235. Six-millimeter sources and ammonia emission were observed in the region by Klein et al. (2005). We detected a weak continuum source toward the IRAS region at 3.6 cm. However, it is shifted about  $\approx 49''$  from the IRAS position. Besides, this continuum source is not spatially coincident with any of the other millimeter sources detected by Klein et al. (2005), the closest one being  $1''$  away. Our calculated physical parameters suggest that this compact source is an H II region with a ZAMS B2 star.

**IRAS 06412-0105** is located toward the WB870 region. A millimeter source was detected in the region by Klein et al. (2005), which was interpreted as a low-mass dust core embedded in the extended emission. Contour maps at 3.6 and 1.3 cm show a source with cometary morphology that has a size of about  $13'' \times 11''$  at 3.6 cm and is spatially coincident with the IRAS source. A similar morphology is also observed at 6 cm, but the compact source seems to split into a double system.

Taking into account the compact and extended emission of the continuum source, we estimated a spectral index of  $\approx -0.2$ , which is interpreted as an optically thin H II region. In addition, H II region models indicate that this source is an UC H II region with Gaussian morphology, associated with a ZAMS O7.5 star.

**IRAS 06567-0355.** Both millimeter and IR sources were detected in this region by Klein et al. (2005) and Zhang & Wu (1996), respectively.  $\text{NH}_3$  (1,1) and (2,2) emission, as well as a bipolar outflow were also reported by Klein et al. (2005) and Wu, Huang & He (1996), respectively.

We detected a nearly spherical 3.6 cm continuum source that is shifted about  $\approx 290''$  from the IRAS source and is not spatially coincident with the millimeter source. In addition, this continuum source was detected at 6 cm, but with a slightly elongated morphology and showing several protuberances. Using the centimeter emission, we calculated a spectral index of  $\approx -0.5$  between 3.6 and 6 cm, which is consistent with non-thermal emission. This spectral index value could be explained by the presence of variability in the flux density, or the continuum source could be a multiple system. Simultaneous and high angular resolution observations will be necessary to confirm its nature.

**IRAS 07299-1651.** A millimeter and infrared sources, separated by  $\approx 2.4''$ , were detected by Klein et al. (2005) and Rosero et al. (2019), respectively. A single continuum source is detected at 3.6 cm in the field, but not at 1.3 cm. It is spatially coincident with the millimeter source, and based on its continuum emission, this source is consistent with an UC H II region maintained by a ZAMS B3 star.

**IRAS 07311-2204** is located toward BRAN 45 region, which has a diameter of  $\approx 25'$  and CO emission (May, Alvarez, & Bronfman 1997). We detected an extended continuum source at 3.6 cm with angular size  $\approx 6''$ . This continuum source is spatially coincident with the IRAS source and lies within the BRAN 45 region. Assuming it to be an H II region and based on its 3.6 cm continuum emission, we found that the ionizing star is a ZAMS B0.5 star.

**IRAS 07427-2400** is a high-mass star-forming region (MacLeod et al. 1998). Trinidad (2011) found a cluster of at least three radio continuum sources, two of which are UC H II regions, while the strongest source is a jet. These sources have also been detected at millimeter wavelengths by Qiu et al. (2009). We detect a continuum source at 3.6 cm; however, we note a peculiar morphology that resembles neither an H II region nor thermal jets. This

fact could be explained as due to the low angular resolution of the observations at 3.6 cm, which do not spatially separate the embedded sources detected by Trinidad (2011).

**IRAS 07528–3441.** Using CS(2–1) and  $^{12}\text{CO}$  observations, Bronfman, Nyman & May (1996) found an UC H II region and a molecular outflow toward IRAS 07528–3441. In addition,  $\text{NH}_3$  (1–1) has been also detected by Urquhart et al. (2011).

The 3.6 cm continuum emission shown in Figure 2 seems to be elongated in the north-south direction, as is also observed at 6 cm. A continuum peak is clearly detected and there is evidence of a weaker second peak. However, the second peak detected at 6 cm is not coincident with the one detected at 3.6 cm. In addition, the continuum emission does not spatially coincide with the UC H II region detected by Bronfman, Nyman & May (1996), which is offset by  $\approx 2'$ . Based on the spectral index ( $\approx 0.15$ ) and the H II region models, we find that this continuum source is consistent with an UC H II region harboring a B1 ZAMS star.

**IRAS 08189–3602** was observed as a radio continuum source by Wouterloot & Brand (1989), while Planck Collaboration et al. (2015) found a compact H II region through mm and sub-mm observations. We detect a continuum source at 3.6 and 1.3 cm with a large angular size of  $\approx 20''$  at 3.6 cm. A strong peak at 3.6 cm is observed, but other less defined peaks are also observed. These peaks are probably not associated with other continuum sources, but rather are irregularities of extended emission. To investigate the possibility of the secondary emission peaks being associated with compact embedded sources, we made contour maps removing the shorter baselines, both at 1.3 and 3.6 cm. However, no additional compact sources were detected.

Considering the 1.3 and 3.6 cm emission of the source, Figure 5 shows that the three H II region models fit the data very well. Based on its morphology and physical parameters, we adopt the cylindrical model. However, spherical or Gaussian models could also be consistent. This UC H II region is separated by  $\approx 15''$  from the compact H II region detected at mm wavelengths by Planck Collaboration et al. (2015).

**IRAS 18094–1823** (G12.20–0.03) is a high-mass star-forming region (Hill et al. 2005) and is not part of the original of the AC295 project. It is located about  $\approx 4'$  to the west of the UC H II region G12.21–0.10 (e.g. de la Fuente et al. 2020a, and references therein). It stands out because the presence of low-resolution VLA emission at 3.6 cm

(size  $\approx 20'$ ) that coincides with IRAS 18094–1823 in the radio-continuum study for G12.21–0.10 presented by de la Fuente et al. (2018). In addition, using 6 cm observations from the CORNISH survey, Kalcheva et al. (2018) suggested that this object is an UC H II region. The 3.6 cm contour map shows a spherical compact source, whose emission is produced by an UC H II region. We found the ionizing star to be a ZAMS B0 star.

**IRAS 19120+1103** (G45.47+0.05) is also not included in the original sample of 104 sources, but VLA low-resolution emission at 3.6 cm was detected in a study by de la Fuente et al. (2020a). Its continuum emission is rather associated with the UC H II region with extended emission G45.45+0.06 (see de la Fuente et al. 2020a, and references therein). This source was confirmed as a star-forming region by the detection of  $\text{H}_2\text{O}$  and OH maser emission by Kim, Kim, & Kim (2019). It was classified as an irregular UC H II region based on its 6 cm emission (Wood & Churchwell 1989). The physical parameters and morphology of the 3.6 cm emission are consistent with a compact H II region, with the central source being a ZAMS O9.5 star.

**IRAS 21306+5540** is located towards S128, which has been studied at radio wavelengths by Ho, Haschick, & Israel (1981) and Fich (1986). Three compact H II regions were found by Ho, Haschick, & Israel (1981), labeled as S128A, S128B, and S128N with exciting stars O6, O6, and O9.5, respectively. In addition, an IR and submillimeter source has been detected by Umana et al. (2008), and the presence of a bipolar outflow in the east-west direction has been reported by Kim, Kim, & Kim (2015).

We detected a nearly compact continuum source at 3.6 cm, with a protuberance toward the north. This compact source was also detected at 6 cm and coincides with the source S128N detected by Ho, Haschick, & Israel (1981). We estimate a spectral index of about  $-1.1$ , which is interpreted as non-thermal emission. Such negative spectral indices are generally associated with extra-galactic sources. However, this continuum source is embedded in a star-forming region and has been catalogued as a compact H II region. We could explain this spectral index due to the variability of the source or to the fact that the continuum emission is not associated with a single source (e.g., a protuberance can be observed at 3.6 cm). Its physical parameters are reported in Table 6, assuming it is an H II region.

**IRAS 21334+5039.** A compact H II region, with a ZAMS B0 star, was discovered in this region through radio continuum observations by Mc-

Cutcheon et al. (1991), which coincides with  $\text{NH}_3$  emission detected by Urquhart et al. (2011). In addition, Obonyo et al. (2019) searched for non-thermal radio emission toward this region, but the results were negative.

We detected one continuum source in the field at 3.6 cm, with a compact spherical morphology. A similar morphology was also observed at 6 cm. However, this source has an offset of  $\approx 60''$  from the compact H II region detected by McCutcheon et al. (1991). We determined a spectral index of about  $-0.55$ , which could indicate a non-thermal nature or variability of the source (observations were carried out with a separation of about ten years). Further simultaneous observations will be necessary to determine its nature.

**IRAS 21413+5442.** Two radio continuum sources have been detected by Miralles, Rodríguez & Scalise (1994) and classified as a compact H II and a UC H II region, respectively. In addition, IR observations by Anandarao et al. (2008) showed the presence of a stellar cluster.

We detected a source in the field at 6, 3.6 and 1.3 cm. The morphology of the source is compact, showing slight protrusions in all three wavelengths. It coincides with the IRAS source and one of the IR sources detected by Anandarao et al. (2008), which was interpreted as a massive young stellar object. However, this continuum source is offset by about  $20'$  from the H II regions reported by Miralles, Rodríguez & Scalise (1994). Using the 1.3, 3.6 and 6 cm flux densities, we obtained a spectral index of 0.85, suggesting that this source is an optically partially thick H II region. By modeling this continuum source as an H II region, we find that its physical parameters are consistent with an UC H II region with Gaussian morphology, harboring a ZAMS O8 star.

**IRAS 22134+5834.**  $\text{NH}_3$  and water maser emission were detected toward the IRAS region by Sunada et al. (2007). We detected a continuum source at 3.6 cm, located about  $3.5''$  from the IRAS source. This source shows a compact spherical morphology, and based on its derived physical parameters from the 3.6 cm emission, it could be classified as an UC H II region with a ZAMS B1 star.

**IRAS 22308+5812** is located towards Sh2-138 (Wouterloot & Brand 1989). A compact H II region was studied by Martín-Hernández et al. (2002) and  $\text{NH}_3$  (1,1) emission was reported by Urquhart et al. (2011).

We detected a continuum source at 3.6 cm with a cometary-like H II region morphology, with its emission peak about  $2''$  from the IRAS source. A similar

morphology was also observed at 6 cm. Based on its spectral index ( $\approx 1.4$ ), physical parameters and morphology observed (Figure 2), we suggest this source is an UC H II region with a ZAMS O7.5 star and a Gaussian distribution (see Figure 5).

**IRAS 23030+5958** is located towards S156 (Lee, Murray, & Rahman 2012) and it is one of the most luminous regions of the sample. Using low angular resolution observations at 6 cm, Israel (1977) found a group of H II regions (S156) with at least two O stars and three B stars.

We detected continuum emission at 3.6 and 1.3 cm, but the morphology does not have a well-defined structure; rather, it shows a complicated morphology with at least three continuum peaks detected at both wavelengths (VLA1, VLA2, and VLA3), aligned in the east-west direction. This morphology is also observed at 6 cm. All continuum peaks are contained in the S156A source and interpreted as an H II region. In general, the morphology of S156A and the other sources detected by Israel (1977) was explained by the quasi-stationary blister type model. Considering that all the emission detected in the field is part of a single H II region and based on its spectral index information and derived physical parameters, we find that its continuum emission is consistent with an optically partially thin UC H II region excited by ZAMS O8 stars.

## REFERENCES

- Anandarao, B. G., Venkata Raman, V., Ghosh, S. K., Ojha, D. K., & Kumar, M. S. N., 2008, MNRAS, 390, 1185, <https://doi.org/10.1111/j.1365-2966.2008.13820.x>
- Anglada, G., Rodríguez, L. F., & Carrasco-González, C., 2018, A&ARv. 26, 3, <https://doi.org/10.1007/s00159-018-0107-z>
- Beuther, H., Schilke, P., Menten, K. M., et al. 2002a, ApJ, 566, 945, <https://doi.org/10.1086/338334>
- Beuther, H., Schilke, P., Gueth, F., et al. 2002b, A&A387, 931, <https://doi.org/10.1051/0004-6361:20020319>
- Beuther, H., Churchwell, E. B., McKee, C. F., & Tan, J. C. 2007, Protostars and Planets V, (Tucson, AZ: UAP), 165, <https://doi.org/10.48550/arXiv.astro-ph/0602012>
- Bronfman, L., Nyman, L.-A., & May, J. 1996, A&AS, 115, 81
- Deeg, H.-J., Brinks, E., Duric, N., Klein, U., & Skillman, E. D. 1993, ApJ, 410, 626, <https://doi.org/10.1086/172780>
- de la Fuente, E., Porras, A., Trinidad, M. A., et al. 2020a, MNRAS, 492, 895, <https://doi.org/10.1093/mnras/stz3482>

- de la Fuente, E., Tafuya, D., Trinidad, M. A., et al. 2020b, *MNRAS*, 497, 4436, <https://doi.org/10.1093/mnras/staa2149>
- de la Fuente, E., Trinidad, M. A., Porras, A., et al. 2018, *RMxAA*, 54, 129
- de Pree, C. G., Rodríguez, L. F., & Goss, W. M. 1995, *RMxAA*, 31, 39
- Fich, M., 1986, *AJ*, 92, 787, <https://doi.org/10.1086/114212>
- Franco, J., Kurtz, S. E., García-Barreto, J. A., et al. 2001, *ApSSS*, 277, 71, <https://doi.org/10.1023/A:1012779627430>
- Franco, J., García-Barreto, J. A., & de la Fuente, E. 2000a, *ApJ*, 544, 277, <https://doi.org/10.1086/317189>
- Franco, J., Kurtz, S., Hofner, P., et al. 2000b, *ApJ*, 542, 143, <https://doi.org/10.1086/312938>
- Franco, J., Tenorio-Tagle, G., & Bodenheimer, P. 1990, *ApJ*, 349, 126, <https://doi.org/10.1086/168300>
- Garay, G. & Lizano, S. 1999, *PASP*, 111, 1049, <https://doi.org/10.1086/316416>
- Hill T., Burton, M. G., Minier, V., et al. 2005, *MNRAS*, 366, 405, <https://doi.org/10.1111/j.1365-2966.2005.09347.x>
- Ho, P. T. P., Haschick, A. D., & Israel, F. P. 1981, *ApJ*, 243, 526, <https://doi.org/10.1086/158617>
- Israel, F. P. 1977, *A&A*, 59, 27
- Jaffe, D. T. & Martín-Pintado, J., 1999, *ApJ*, 520, 162, <https://doi.org/10.1086/307440>
- Kalcheva, I. E., Hoare, M. G., Urquhart, J. S., et al. 2018, *A&A*, 615, 103, <https://doi.org/10.1051/0004-6361/201832734>
- Kim, K.-T., Kim, W.-J., & Kim, C.-H. 2015, *JKAS*, 48, 365, <https://doi.org/10.5303/JKAS.2015.48.6.365>
- Kim, W.-J., Kim, K.-T., & Kim, K.-T. 2019, *ApJS*, 244, 2, <https://doi.org/10.3847/1538-4365/ab2fc9>
- Klein, R., Posselt, B., Schreyer, K., Forbrich, J., & Henning, Th. 2005, *ApJS*, 161, 361, <https://doi.org/10.1086/496962>
- Kurtz, S. & Franco, J. 2002, *RMxAC*, 12, 16
- Kurtz, S., Churchwell, E., & Wood, D. O. S. 1994, *ApJS*, 91, 659, <https://doi.org/10.1086/191952>
- Launhardt, R., Loinard, L., Dzib, S. A., et al. 2022, *ApJ*, 931, 43, <https://doi.org/10.3847/1538-4357/ac5b09>
- Lee, E. J., Murray, N., & Rahman, M. 2012, *ApJ*, 752, 146, <https://doi.org/10.1088/0004-637X/752/2/146>
- Lu, X., Zhang, Q., Liu, H. B., Wang, J., & Gu, Q. 2014, *ApJ*, 790, 84, <https://doi.org/10.1088/0004-637X/790/2/84>
- Lumsden, S. L., Hoare, M. G., Urquhart, J. S., et al. 2013, *ApJS*, 208, 11, <https://doi.org/10.1088/0067-0049/208/1/11>
- MacLeod, G. C., Scalise, E. Jr., Saedt, S., Galt, J. A., & Gaylard, M. J. 1998, *AJ*, 116, 1897, <https://doi.org/10.1086/300538>
- Martín-Hernández, N. L., Peeters, E., Morisset, C., et al. 2002, *A&A*, 381, 606, <https://doi.org/10.1051/0004-6361:20011504>
- Maud, L. T., Moore, T. J. T., Lumsden, S. L., et al. 2015, *MNRAS*, 453, 645, <https://doi.org/10.1093/mnras/stv1635>
- May, J., Alvarez, H., & Bronfman, L. 1997, *A&A*, 327, 325
- McCutcheon, W. H., Dewdney, P. E., Purton, C. R., & Sato, T. 1991, *AJ*, 101, 1435, <https://doi.org/10.1086/115776>
- McMullin, J. P., Waters, B., Schiebel, D., Young, W., & Golap, K., 2007, *ASPC 376*, *Astronomical Data Analysis Software and Systems*, ed. R. A. Shaw, F. Hill, & D. J. Bell, 127
- Miralles, M. P., Rodríguez, L. F., & Scalise, E. 1994, *ApJS*, 92, 173, <https://doi.org/10.1086/191965>
- Mookerjee, B., Sandell, G., Stutzki, J., & Wouterloot, J. G. A., 2007, *A&A*, 473, 485, <https://doi.org/10.1051/0004-6361:20077878>
- Motte, F., Bontemps, S., & Louvet, F. 2018, *ARA&A*, 56, 41, <https://doi.org/10.1146/annurev-astro-091916-055235>
- Navarrete, F., Damineli, A., Barbosa, C. L., & Blum, R. D. 2015, *MNRAS*, 450, 4364, <https://doi.org/10.1093/mnras/stv914>
- Obonyo, W. O., Lumsden, S. L., Hoare, M. G., et al. 2019, *MNRAS*, 486, 3664, <https://doi.org/10.1093/mnras/stz1091>
- Olnon, F. M., 1975, *A&A*, 39, 217
- Panagia, N. 1973, *AJ*, 78, 929, <https://doi.org/10.1086/111498>
- Phillips, J. P. 2007, *MNRAS*, 380, 369, <https://doi.org/10.1111/j.1365-2966.2007.12078.x>
- Phillips, J. P. 2008, *NewA*, 13, 60, <https://doi.org/10.1016/j.newast.2007.06.013>
- Planck Collaboration, Arnaud, M., Atrio-Barandela, et al. 2015, *A&A*, 573, 6, <https://doi.org/10.1051/0004-6361/201423836>
- Preite-Martínez, A. 1988, *A&AS*, 76, 317
- Qiu, K., Zhang, Q., Wu, J., & Chen, H.-R. 2009, *ApJ*, 696, 66, <https://doi.org/10.1088/0004-637x/696/1/66>
- Reynolds, S. P. 1986, *ApJ*, 304, 713, <https://doi.org/10.1086/164209>
- Rodríguez, L. F., González, R. F., Montes, G., et al. 2012, *ApJ*, 755, 152, <https://doi.org/10.1088/0004-637X/755/2/152>
- Rosero, V., Tanaka, K. E. I., Tan, J. C., et al. 2019, *ApJ*, 873, 20, <https://doi.org/10.3847/1538-4357/ab0209>
- Rudolph, A. L., Brand, J., De Geus, E. J., & Wouterloot, J. G. A. 1996, *ApJ*, 458, 653, <https://doi.org/10.1086/176847>
- Schraml, J. & Mezger, P. G. 1969, *ApJ*, 156, 269, <https://doi.org/10.1086/149964>
- Sewilo, M., Churchwell, E., Kurtz, S., Goss, W. M., & Hofner, P. 2011, *ApJS*, 194, 44, <https://doi.org/10.1086/176847>

- 10.1088/0067-0049/194/2/44  
 \_\_\_\_\_ . 2008, ApJ, 681, 350, <https://doi.org/10.1086/588422>
- \_\_\_\_\_ . 2004, ApJ, 605, 285, <https://doi.org/10.1086/382268>
- Snell, R. L., Carpenter, J. M., & Heyer, M. H. 2002, ApJ, 578, 229, <https://doi.org/10.1086/342424>
- Sridharan, T. K., Beuther, H., Schilke, P., Menten, K. M., & Wyrowski, F. 2002, ApJ, 566, 931, <https://doi.org/10.1086/338332>
- Sunada, K., Nakazato, T., Ikeda, N., et al. 2007, PASJ, 59, 1185, <https://doi.org/10.1093/pasj/59.6.1185>
- Tapia, M., Persi, P., Bohigas, J., & Ferrari-Toniolo, M. 1997, AJ, 113, 1769, <https://doi.org/10.1086/118390>
- Trinidad, M. A., Curiel, S., Cantó, J., et al. 2003, ApJ, 589, 386, <https://doi.org/10.1086/374618>
- Trinidad, M. A., Rodríguez, T., & Rodríguez, L. F. 2009, ApJ, 706, 244, <https://doi.org/10.1088/0004-637x/706/1/244>
- Trinidad, M. A. 2011, AJ, 142, 147, <https://doi.org/10.1088/0004-6256/142/5/147>
- Umana, G., Leto, P., Trigilio, C., et al. 2008, A&A, 482, 529, <https://doi.org/10.1051/0004-6361:20078796>
- Urquhart, J. S., Hoare, M. G., Purcell, C. R., et al. 2009, A&A, 501, 539, <https://doi.org/10.1051/0004-6361/200912108>
- Urquhart, J. S., Morgan, L. K., Figura, C. C., et al. 2011, MNRAS, 418, 1689, <https://doi.org/10.1111/j.1365-2966.2011.09594>
- Williams, S. J., Fuller, G. A., & Sridharan, T. K. 2004, A&A, 417, 115, <https://doi.org/10.1051/0004-6361:20031733>
- Wood, D.O.S. & Churchwell, E. 1989, ApJS, 69, 831, <https://doi.org/10.1086/191329>
- Wouterloot, J. G. A. & Brand, J. 1989, A&AS, 80, 149
- Wu, Y. W., Reid, M. J., Sakai, N., et al. 2019, ApJ, 874, 94, <https://doi.org/10.3847/1538-4357/ab001a>
- Wu, Y., Huang, M., & He, J. 1996, A&AS, 115, 283
- Yao, Y., Ishii, M., Nagata, T., Nakaya, H., & Sato, S. 2000, ApJ, 542, 392, <https://doi.org/10.1086/309515>
- Zhang, W.-H. & Wu, Y.-F. 1996, ChA&A, 20, 326, [https://doi.org/10.1016/0275-1062\(96\)00046-X](https://doi.org/10.1016/0275-1062(96)00046-X)

Eduardo de la Fuente: Departamento de Física, CUCEI, Blvd. Gral. Marcelino García Barragán 1421, Olímpica, 44430, Guadalajara, Jalisco, México ([eduardo.delafuente@academicos.udg.mx](mailto:eduardo.delafuente@academicos.udg.mx)).

Josep M. Masqué: Departamento de Astronomía, Universidad de Guanajuato, Apartado Postal 144, 36000, Guanajuato, Guanajuato, México ([jmasque@ugto.mx](mailto:jmasque@ugto.mx)).

Daniel Quiroga-González: Universidad Autónoma Metropolitana-Iztapalapa, México ([dquirogag@gmail.com](mailto:dquirogag@gmail.com)).

Tatiana Rodríguez-Esnard: Instituto de Geofísica y Astronomía de la República de Cuba, calle 212 # 2906 e/ 29 y 31 la Coronela, la Lisa 11600, C. Habana, Cuba ([tatiana@iga.cu](mailto:tatiana@iga.cu)) ([esnard73@gmail.com](mailto:esnard73@gmail.com)).

Miguel Ángel Trinidad: Departamento de Astronomía, Universidad de Guanajuato, Apdo. Postal 144, 36000 Guanajuato, México ([trinidad@ugto.mx](mailto:trinidad@ugto.mx)).